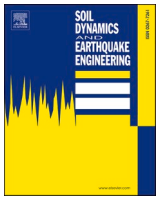
Soil Dynamics and Earthquake Engineering 212 (2027) 110740



Contents lists available at ScienceDirect

Soil Dynamics and Earthquake Engineering

journal homepage: www.elsevier.com/locate/soildyn



Bayesian framework for uncertainty-informed seismic capacity modeling of embankment dams for fragility and risk assessment

Surya Prakash, P. Anbazhagan *

Department of Civil Engineering, Indian Institute of Science, Bangalore, Karnataka, 560012, India

ARTICLE INFO

Keywords:
Embankment dams
Bayesian framework
Seismic capacity
Fragility curves
Uncertainty quantification

ABSTRACT

Seismic fragility assessment of embankment dams requires probabilistic models for seismic demand and capacity, where capacity defines damage-state (DS) exceedance as a function of engineering demand parameter (EDP). Conventional capacity models are often deterministic or simplified, failing to capture uncertainty in the EDP–DS relationship. This study introduces a Bayesian framework for uncertainty-informed capacity models and applies it to fragility and risk analysis. Capacity relationships are inferred from earthquake case histories by assigning DSs from observed damage and using relative crest settlement (RS) as the EDP. DS-specific functions are estimated via Bayesian probit regression with Markov Chain Monte Carlo sampling, giving posterior distributions of median capacity and dispersion. The framework is demonstrated on a 16 m high embankment dam, combining Bayesian models with probabilistic seismic demand models (PSDMs) from nonlinear dynamic finite-element analyses across intensity measures (IMs) to derive fragility curves and the expected damage index (EDI). Compared to deterministic (PF) and non-Bayesian probabilistic (HR) models, Bayesian models preserve median capacity while increasing dispersion, propagating capacity uncertainty, and raising fragility and EDI sensitivity across DS. Capacity-uncertainty influence varies with DS: Minor shows the largest deviations from the deterministic case (approx. 0.28–0.30 across IMs), followed by Moderate (0.23–0.26) and Severe (0.20–0.23), matching the posterior dispersion, largest for Minor and smallest for Severe. Sensitivity is comparable across IMs, VRMS slightly smaller than PGA and PGV. Capacity dominates Minor, contributes substantially to Moderate, and remains larger for Severe DS. PF yields EDI 29–30% and HR 1–3% higher than Bayesian.

1. Introduction

Embankment dams provide hydropower, irrigation, flood control, and water storage, and are essential to water resources and energy systems [1,2]. Ensuring the seismic safety of embankment dams is a major concern for infrastructure management, given their strategic importance and the potentially severe consequences of failure. Unlike rigid concrete structures, embankment dams usually exhibit permanent deformations rather than sudden, brittle collapse under strong earthquake shaking [3–5]. Geotechnical investigations and post-earthquake reconnaissance consistently show that seismic damage in embankments manifests as gradual sliding, settlement, and cracking [4–7]. Accordingly, deformation-based performance measures are widely adopted for seismic performance and risk assessment of embankment dams [5,8,9].

Among various deformation indicators, relative crest settlement (RS), defined as earthquake-induced vertical crest settlement normalized by dam height, has emerged as a primary empirical damage indicator for embankment dams [10,11]. RS is frequently reported in historical earthquake case histories and reconnaissance studies and represents one of the most readily available engineering demand parameters (EDPs) for earth dams [8]. As a physically interpretable measure of global dam deformation, increasing RS has been shown to correlate systematically with progressively more severe damage, including cracking, slumping, and loss of freeboard [8,12]. The broad availability of RS observations across dam types and seismic events has led to its widespread use in fragility analysis and performance-based earthquake engineering (PBEE) applications for embankment dams [10,12,13]. Numerous studies have demonstrated that observed earthquake damage scales directly with RS [8,10,12]. This supports the use of RS as a practical, physically interpretable indicator of deformation, without requiring explicit modeling of detailed failure mechanisms [8, 12].

Within the PBEE framework, seismic capacity models quantify the

* Corresponding author.
E-mail addresses: suryaprakas1@iisc.ac.in (S. Prakash), anbazhagan@iisc.ac.in (P. Anbazhagan).

https://doi.org/10.1016/j.soildyn.2026.110740
Received 20 February 2026; Received in revised form 29 September 2026; Accepted 30 September 2026
0267-7261/© 2026 Elsevier Ltd. All rights are reserved, including those for text and data mining, AI training, and similar technologies.

damage-state (DS) exceedance as a function of an EDP, such as RS [11]. Early seismic capacity formulations for embankment dams relied primarily on deterministic deformation thresholds. For example, Pells and Fell [9] associated Minor, Moderate, and Severe damage with RS values of approximately 0.05%, 0.2%, and 1.0%, respectively. While such threshold-based approaches provide simple and transparent screening tools, they assume abrupt transitions between DSs and do not reflect the substantial scatter observed in post-earthquake performance data. In practice, recorded RS values from past earthquakes exhibit significant variability under similar shaking intensities, indicating that single-valued deformation limits are insufficient to accurately represent seismic capacity.

More recent research has developed probabilistic seismic capacity models to overcome these constraints, in which DS-dependent RS capacities are described by median values and related dispersions derived from earthquake case histories [11]. These empirical and semi-empirical models typically model seismic capacity using lognormal distributions of RS for each DS, thereby explicitly accounting for data scatter and uncertainty. For instance, He and Rathje [11] developed RS-based fragility frameworks in which statistical seismic capacity models were derived directly from observed dam performance. However, in many existing fragility formulations, capacity uncertainty and seismic demand variability are incorporated within aggregate dispersion terms, limiting transparency regarding their relative contributions to overall fragility dispersion [10,13,14].

Fragility curves express the probability of exceeding a specified DS as a function of a ground-motion intensity measure (IM) [15]. Within PBEE, standardized procedures for constructing fragility functions are based on experimental, analytical, empirical, and updated observational evidence [16]. Probabilistic Seismic Demand Models (PSDMs) relating EDP to the IM are combined with seismic capacity models to create analytical fragility models, which usually assume lognormal functional forms [6,11,17]. Fragility relationships for embankment dams have been developed using the conventional IM, peak ground acceleration (PGA), and optimal velocity-based IMs such as peak ground velocity (PGV) and root mean square velocity (VRMS), with RS adopted as the EDP [10–12,14]. Fragility functions for embankment dams have also been developed using multiple-stripe analysis, classical regression, and other numerical and statistical approaches [18]. Jin and Chi [18] demonstrated that increased ground-motion sampling reduces uncertainty in both the mean and dispersion of RS, highlighting the important role of demand variability in fragility estimation. Building on these fragility formulations, recent studies have used advanced numerical and surrogate-based methods to characterize seismic demand in embankment-type geotechnical systems. Nonlinear finite-element analyses have examined liquefaction-induced deformation, pore-pressure generation, damage progression, and the effects of real and synthetic ground motions on settlement and fragility [19,20]. Gaussian-process surrogates have also been used to reduce the computational cost of repeated simulations [21], while mainshock–aftershock studies have evaluated cumulative damage and the evolution of fragility in liquefiable embankment–foundation systems [22]. These studies primarily advance demand-side modeling and do not directly address uncertainty in deformation-based seismic capacity relationships inferred from sparse earthquake case-history data.

Bayesian inference offers a systematic and theoretically coherent framework for managing uncertainty, particularly when model parameters must be inferred from sparse and heterogeneous observational datasets [23–26]. Within a Bayesian framework, DS dependent RS capacity parameters, such as dispersion and median capacity, can be represented as random variables with specified prior distributions. This approach enables the integration of sparse, heterogeneous earthquake case-history data, facilitates the explicit separation of aleatory variability and epistemic uncertainty, and yields posterior distributions of capacity parameters through probabilistic inference [27,28]. Bayesian methods have been effectively utilized in structural reliability and seismic risk evaluation to revise fragility and capacity correlations within a coherent probabilistic framework [15,29–31]. PSDMs can be integrated with Bayesian capacity models to generate fragility curves that incorporate both capacity and demand uncertainty, yielding smooth, physically realistic DS exceedance relationships [18,32]. These uncertainty-informed capacity models can then be consistently integrated with PSDMs to propagate capacity uncertainty into fragility estimates [31]. However, for embankment dams where available case-history data are often sparse, heterogeneous, and unevenly distributed across DSs, the application of Bayesian inference to deformation-based seismic capacity modeling within the PBEE framework remains limited [33,34]. Despite advances in probabilistic fragility modeling, existing deformation-based seismic capacity models for embankment dams typically rely on deterministic thresholds [9] or fixed dispersion parameters [11], limiting explicit treatment of capacity uncertainty and its propagation into fragility and risk metrics.

This study develops a Bayesian framework for uncertainty-informed seismic capacity modeling of embankment dams, using relative crest settlement (RS) as the engineering demand parameter (EDP). Damage-state (DS) dependent capacity relationships are inferred from sparse, heterogeneous earthquake case-history data using Bayesian probit regression implemented via Markov Chain Monte Carlo (MCMC) sampling. This approach yields full posterior distributions of deformation-capacity parameters, enabling explicit and quantitative treatment of capacity uncertainty associated with observational damage data. The inferred Bayesian capacity models are integrated with probabilistic seismic demand models (PSDMs) formulated using the conventional IM (PGA) and velocity-based IMs (PGV and VRMS) to derive uncertainty-consistent fragility curves and risk metrics, such as the Expected Damage Index (EDI). The proposed framework enables analytical propagation of posterior uncertainty in the inferred capacity parameters through the fragility formulation, while maintaining a clear separation between capacity uncertainty and demand-driven aleatory variability. As a result, the derived fragility curves provide a mechanistically and probabilistically consistent basis for deformation-based seismic performance evaluation and risk assessment of embankment dams. The framework is demonstrated through a case study of a 16 m high embankment dam analyzed using nonlinear dynamic finite-element simulations subjected to a suite of recorded ground motions. The case study serves to demonstrate the proposed framework and evaluate how probabilistically inferred Bayesian capacity relationships influence fragility characteristics, damage-state exceedance probabilities, and derived risk metrics.

The novel contributions of this study are as follows: (i) Development of a continuous, data-driven probabilistic seismic capacity model for embankment dams that replaces deterministic RS thresholds with statistically inferred DS exceedance relationships derived from earthquake case-history data; (ii) Explicit Bayesian treatment of capacity uncertainty in DS capacity parameters using MCMC sampling, producing full joint posterior distributions rather than fixed parameter estimates and formally separating capacity uncertainty from seismic demand uncertainty; (iii) Consistent integration of posterior capacity uncertainty with probabilistic seismic demand models formulated using alternative candidate IMs, enabling uncertainty-consistent derivation of fragility relationships; (iv) Analytical decomposition of fragility dispersion into demand-related and capacity-related components through capacity uncertainty propagation and sensitivity analysis, providing insight into the dominant sources of fragility variability; (v) Evaluation of engineering and decision-relevant implications, including the influence of alternative capacity representations on fragility estimates, exceedance probabilities, and derived seismic risk metrics; and (vi) comparative assessment of the proposed Bayesian fragility formulations against deterministic threshold-based and non-Bayesian probabilistic capacity models within PBEE framework.

2. Case history dataset for seismic capacity models

This study uses 94 earthquake case histories of embankment dams compiled by He and Rathje [11] and available through the associated DesignSafe-CI database [35]. The dataset provides an empirical basis for deformation-based seismic capacity modeling, using relative crest settlement (RS) as the engineering demand parameter (EDP). Its finite size and uneven distribution across DS categories contribute to uncertainty in the inferred capacity parameters, which is explicitly quantified through the Bayesian framework developed in Section 3.

2.1. Damage-state classification and dataset composition

Damage state (DS) classification follows He and Rathje [11] and is based on post-earthquake reconnaissance observations. Five ordered DSs are defined, ranging from no damage to collapse, based on observed cracking, settlement, leakage, and sliding. Minor damage involves small movements and cracks of a few centimeters; Moderate damage involves more extensive cracking and noticeable movements that require repair; Severe damage involves significant settlement, major cracking, and possible leakage; and Collapse involves major sliding or overtopping, requiring reconstruction [11]. Of the 94 cases, 15 correspond to no damage (DS1), 49 to Minor damage (DS2), 19 to Moderate damage (DS3), 8 to Severe damage (DS4), and 3 to Collapse (DS5) [11]. As reconnaissance-based classifications may involve subjective interpretation, additional uncertainty is inherent in DS assignment.

2.2. Dataset characteristics and heterogeneity

Fig. 1 summarises the principal characteristics of the case-history dataset. The available variables include dam height (H_D), dam type (DT), earthquake magnitude (M_w), relative crest settlement (RS), and qualitative damage descriptions. The cases span a broad range of seismic and geometric conditions, with M_w ranging from approximately 4.9 to 9.1 and H_D from about 6 to 147m. Substantial overlap is observed in the M_w and H_D distributions across the DS categories. The RS relationships also exhibit broad scatter, with no strong monotonic dependence on either M_w or H_D individually. Higher DSs are generally associated with larger RS values; however, overlap remains between adjacent categories, reflecting the heterogeneity of the case histories and uncertainty in reconnaissance-based damage classification. The observed variability reflects differences in seismic loading, dam geometry, material properties, foundation conditions, construction characteristics, and local site conditions. Several of these attributes, including detailed ground-motion IMs, shaking duration, frequency content, and site-response parameters, are not consistently documented across the dataset. The

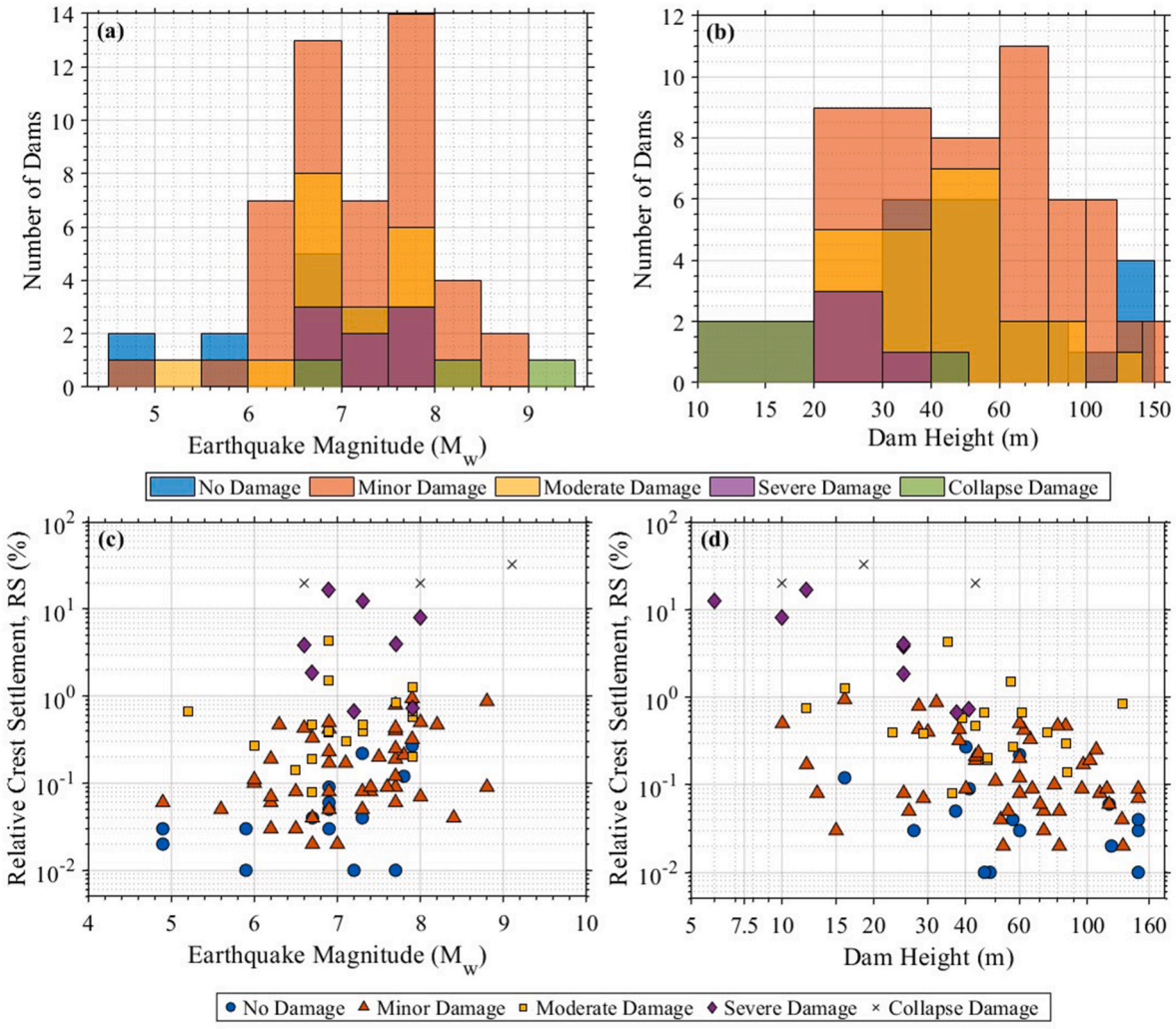


Fig. 1. Characteristics of the embankment-dam case-history dataset. (a) Earthquake moment magnitude (M_w) by damage state. (b) Dam height by damage state. (c) Relative crest settlement (RS) versus M_w. (d) Relative crest settlement (RS) versus dam height. RS is plotted on a logarithmic scale in (c) and (d), and dam height is plotted on a logarithmic scale in (d). Colors and symbols denote the observed damage states. (For interpretation of the references to colour in this figure legend, the reader is referred to the Web version of this article.)

case histories therefore represent a heterogeneous empirical population rather than a geometry or site-specific dam configuration. Within the Bayesian capacity model, unresolved case to case variability is represented by the DS specific capacity dispersion, while uncertainty in estimating the capacity parameters from the finite dataset is quantified by their posterior distributions. The resulting dataset characteristics provide the basis for the Bayesian formulation presented in Section 3 and the threshold-specific calibration described in Section 4.

3. Proposed Bayesian capacity modelling framework

This section presents a Bayesian framework for quantifying the deformation-based seismic capacity of embankment dams, explicitly accounting for capacity dispersion and posterior uncertainty in the inferred capacity parameters. The proposed framework formulates seismic capacity probabilistically within a Bayesian inference setting, enabling explicit, data-informed quantification of capacity uncertainty in DS specific capacity parameters inferred from earthquake case-history data. The resulting posterior distributions provide a comprehensive characterisation of seismic capacity uncertainty and support consistent propagation into fragility and seismic risk analyses. The framework integrates: (i) DS exceedance modeling, (ii) lognormal representation of RS capacity, (iii) Bayesian inference using multi-chain Markov Chain Monte Carlo (MCMC) sampling, and (iv) diagnostic tools for assessing convergence and predictive adequacy [36,37]. Fig. 2 illustrates the overall workflow of the proposed Bayesian capacity modeling framework. Each DS threshold is modeled using an independent Bayesian probit regression, consistent with common threshold-specific capacity modeling approaches [38,39].

3.1. Damage state exceedance definition

For probabilistic modeling, the RS is strictly positive and is therefore transformed into logarithmic space to stabilize variance and ensure consistency with the assumed lognormal capacity model. The transformation is defined as:

$$Z = \ln(RS) \tag{1}$$

where Z denotes the logarithm of the observed RS. Observed DS are represented using a DS exceedance formulation. For each damage threshold k, a binary exceedance indicator $y_i(k)$ is defined for the i^{th} case history as:

$$y_i(k) = \begin{cases} 1, if\ DS_i \geq k \\ 0, if\ DS_i < k \end{cases} \tag{2}$$

where DS_i denotes the observed DS for the i^{th} record. This formulation converts ordinal DS classifications into threshold-specific binary outcomes, enabling the use of probit regression within a Bayesian inference framework [40,41]. Importantly, RS is not used to deterministically assign DSs. Instead, RS serves as a conditioning variable that governs the probability of exceeding a given damage threshold. For a record with observed damage state DS_i, the exceedance indicator is set to $y_i^{(k)} = 1$ for every modeled threshold $k \leq DS_i$ and to $y_i^{(k)} = 0$ for every modeled threshold $k > DS_i$. This formulation fully uses the ordered nature of the observed DSs, avoids the circularity inherent in deterministic threshold-based assignment methods, and enables probabilistic inference of continuous DS transition behavior directly from empirical evidence.

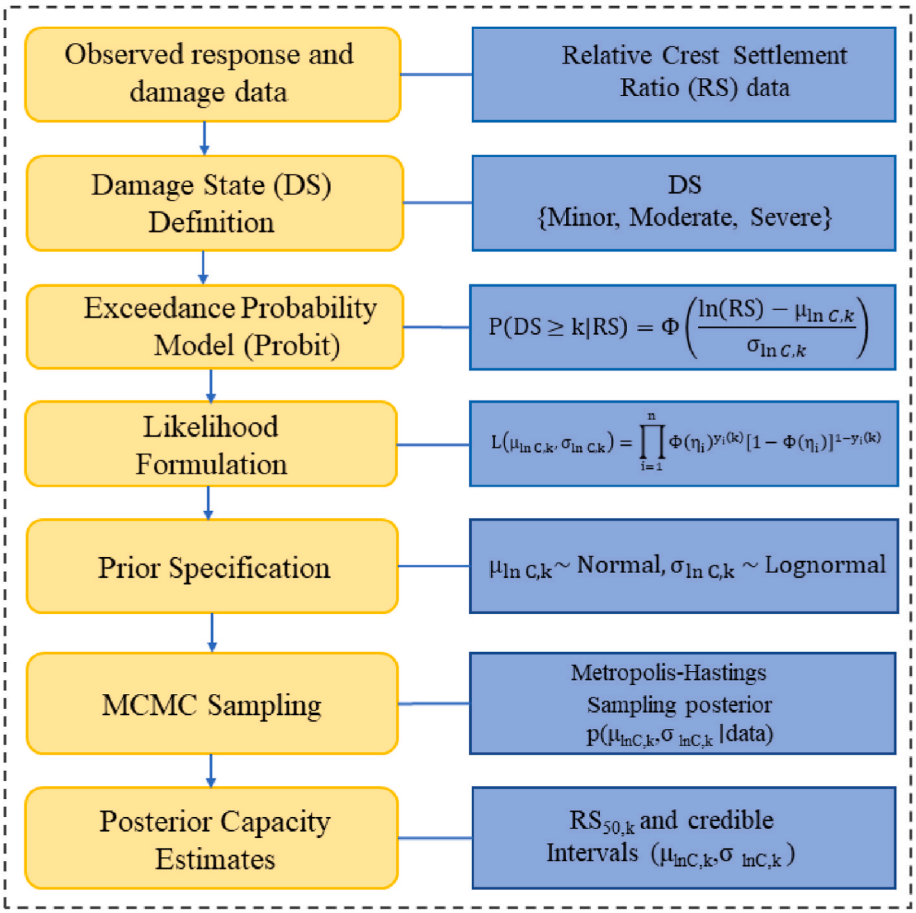


Fig. 2. Proposed Bayesian framework for seismic capacity modeling.

3.2. Seismic capacity model

The deformation capacity associated with each damage threshold is assumed to follow a lognormal distribution. Let C_k denote the random RS-based deformation capacity corresponding to damage threshold k. The conditional probability of exceeding k^{th} DS given an observed RS is expressed as:

$$P(DS \geq k|RS) = P(C_k \leq RS) = \Phi\left(\frac{\ln(RS) - \mu_{\ln C,k}}{\sigma_{\ln C,k}}\right) \quad (3)$$

where $\mu_{\ln C,k}$ and $\sigma_{\ln C,k}$ are the logarithmic median and dispersion of the RS capacity for damage threshold k, and $\Phi(\cdot)$ is the standard normal cumulative distribution function. The subscript k denoting the damage threshold is retained in the general formulations and omitted in the results, tables, and figures, in which the DS is identified explicitly; in those contexts, the parameters are denoted μ_{lnC} and σ_{lnC}. The median deformation capacity in physical space is given by:

$$RS_{50,k} = e^{\mu_{\ln C,k}} \quad (4)$$

This lognormal formulation ensures non-negativity of RS, is consistent with observed deformation behavior of embankment dams, and provides a mathematically convenient basis for combining capacity and demand uncertainty in fragility analysis [11,17,42]. In this representation, $\sigma_{lnC,k}$ characterizes the residual dispersion in the RS–DS relationship, including the combined influence of unresolved case-to-case variability and reconnaissance-based classification uncertainty. Posterior uncertainty in $\mu_{lnC,k}$ and $\sigma_{lnC,k}$ inferred through Bayesian updating represents uncertainty in the capacity parameters arising from finite, heterogeneous calibration data.

3.3. Likelihood function

Let RS_i denote the observed RS for the i^{th} record, and let $y_i(k)$ be the corresponding binary DS exceedance indicator for threshold k. Assuming conditional independence among observations, the likelihood function for the capacity parameters $\mu_{\ln C,k}$ and $\sigma_{\ln C,k}$ is given by:

$$L(\mu_{ln\ C,k}, \sigma_{ln\ C,k}) = \prod_{i=1}^{n} [\Phi(\eta_i)]^{y_i(k)}[1 - \Phi(\eta_i)]^{1-y_i(k)} \quad (5)$$

with

$$\eta_i = \frac{ln\ RS_i - \mu_{ln\ C,k}}{\sigma_{ln\ C,k}} \quad (6)$$

where n denotes the number of observations associated with damage threshold k. This likelihood represents the joint probability of observing the binary DS exceedance outcomes under the assumed lognormal capacity model and forms the basis for Bayesian inference of the capacity parameters [40,41].

3.4. Prior distributions

Weakly informative prior distributions are adopted to stabilize inference while allowing the data to dominate posterior estimates [43]. The priors specified in Eq. (7) are referred to hereafter as the Baseline prior and are used for the main Bayesian capacity analysis. The logarithmic median capacity ($\mu_{ln\ C,k}$) is assigned a normal prior with large variance, while the dispersion parameter ($\sigma_{ln\ C,k}$) is assigned a lognormal prior to enforce positivity:

$$\mu_{\ln C,k} \sim \mathcal{N}(0, 10^2), \ln \sigma_{\ln C,k} \sim \mathcal{N}(\ln 0.5, 1^2) \quad (7)$$

The baseline normal prior on $\mu_{ln\ C,k}$ spans several orders of magnitude in RS, ensuring minimal prior influence on posterior inference. The baseline lognormal prior on $\sigma_{ln\ C,k}$ reflects plausible variability observed in prior probabilistic capacity and fragility studies while preventing nonphysical values. These priors are selected to improve numerical stability of the Bayesian inference while remaining sufficiently broad relative to the likelihood derived from the available case-history data [28,40,41]. They reflect conventional modeling practice rather than derivation from formal reference-prior theory [40]. A prior sensitivity analysis is presented in Section 3.7 to verify that these priors are weakly informative in practice for the available case-history data.

3.5. Posterior inference

Bayes' theorem yields the posterior distribution of the capacity parameters:

$$p(\mu_{\ln C,k}, \sigma_{\ln C,k}|y) \propto L(\mu_{\ln C,k}, \sigma_{\ln C,k})\ p(\mu_{\ln C,k})\ p(\sigma_{\ln C,k}) \quad (8)$$

where y denotes the vector of observed binary exceedance outcomes, $p(\mu_{\ln C,k})$ and $p(\sigma_{\ln C,k})$ are the prior distributions. Posterior inference is performed using a Metropolis–Hastings MCMC algorithm [44,45]. Separate Bayesian seismic capacity models are estimated for each DS threshold using multiple independent MCMC chains reflecting the low dimensionality of the parameter space comprising the capacity median and dispersion parameters. At each iteration, candidate values of $\mu_{\ln C,k}$ and $\sigma_{\ln C,k}$ are proposed and accepted with probabilities proportional to the ratios of their posterior densities. Chains are run for a fixed number of iterations with an initial burn-in discarded and thinning applied to the post burn-in draws before samples are pooled across chains for inference. The resulting MCMC samples represent draws from the joint posterior distribution of the capacity parameters from which posterior medians, credible intervals, and other uncertainty measures are directly computed [46].

3.6. Diagnostic measures

Model adequacy and sampling performance are evaluated using a suite of complementary diagnostic measures. For each DS capacity model convergence robustness is assessed using MCMC diagnostics. Chain convergence and mixing are evaluated through trace plots and autocorrelation functions (ACF) which provide qualitative evidence of stationarity and adequate exploration of the posterior distribution [46]. Sampling efficiency is quantified using the Effective Sample Size (ESS), which measures the reduction in independent information due to autocorrelation and provides a quantitative indicator of the reliability of posterior summaries [47]. Predictive adequacy is evaluated using the Widely Applicable Information Criterion (WAIC) which estimates out-of-sample predictive performance while accounting for model complexity and posterior uncertainty [47]. In addition, posterior predictive checks (PPCs) compare observed DS exceedance frequencies with distributions generated from the posterior predictive model enabling direct assessment of the model's ability to reproduce key features of the empirical data [27,36]. Collectively, these diagnostics ensure that the inferred Bayesian seismic capacity models provide a statistically robust and coherent probabilistic representation of RS based deformation capacity across modeled DSs thresholds, supporting reliable fragility and seismic risk assessment.

3.7. Prior sensitivity assessment

Prior sensitivity is assessed to determine whether posterior estimates of the deformation-capacity parameters are unduly influenced by prior specification, particularly given the limited, heterogeneous, and unevenly distributed damage-state data [48,49]. The assessment also examines whether the Baseline prior specified in Section 3.4 can be regarded as weakly informative in practice for the available case-history data.

The sensitivity assessment is implemented by re-estimating the

Bayesian capacity models under multiple alternative prior specifications while holding the likelihood formulation, calibration dataset, and MCMC sampling settings fixed. Three prior cases are considered: (i) the Baseline prior specified in Eq. (7), (ii) a Diffuse prior representing reduced prior information and increased variance, and (iii) a Moderately informative prior reflecting mild prior belief while remaining permissive relative to the information content of the data. The statistical models adopted for each prior case are summarised in Table 1. These alternative priors are selected to span a plausible range of deformation capacity assumptions reported in probabilistic capacity and fragility studies while remaining physically reasonable. For each prior specification independent multi-chain MCMC simulations are performed for all modeled DS thresholds, and the resulting posterior medians and 95% credible intervals are compared across priors.

4. Capacity modeling results

The Bayesian framework presented in Section 3 was applied to the case-history dataset described in Section 2 to infer deformation-based seismic capacity relationships. RS was adopted as the conditioning variable because it directly represents the deformation associated with the observed damage outcomes. The remaining variables in the dataset including dam height, dam type, and earthquake magnitude, were used to characterize dataset heterogeneity but were not introduced as explanatory variables in the capacity models. Likewise, the incompletely documented loading, foundation, and site-related variables discussed in Section 2.2 were not included as calibration covariates.

Of the 94 case histories, all DS1–DS4 records were retained, resulting in a calibration dataset of 91 cases. The 15 DS1 records were incorporated as non-exceedance observations to constrain the onset of Minor damage, although no separate capacity relationship was developed for DS1 because it represents the no-damage condition. The three DS5 collapse records were excluded because their limited number precluded reliable statistical inference and because collapse represents post-instability behavior rather than progressive deformation-controlled damage. Capacity relationships were therefore calibrated independently for the $DS \geq 2$, $DS \geq 3$, and $DS \geq 4$ exceedance thresholds, corresponding to Minor, Moderate, and Severe damage, respectively. Application of Eq. (2) yielded 15 non-exceedances and 76 exceedances for $DS \geq 2$, 64 non-exceedances and 27 exceedances for $DS \geq 3$, and 83 non-exceedances and 8 exceedances for $DS \geq 4$. Thus, every retained case history contributed either an exceedance or a non-exceedance observation to each threshold-specific Bayesian model. The resulting capacity relationships, posterior parameter estimates, convergence diagnostics, posterior predictive consistency checks, and prior-sensitivity analyses are presented in the following subsections.

4.1. Empirical capacity models

Fig. 3 presents the empirical relationships between RS and the probability of exceedance for the Minor, Moderate, and Severe DSs. The individual binary observations illustrate the case to case scatter whereas the bin-averaged exceedance rates show the progressive increase in damage probability with increasing deformation. This indicates that damage occurs over a range of RS values rather than at a single deterministic threshold. In Fig. 3a, the binary observations plotted at zero correspond to the 15 DS1 records retained as non-exceedances and constrain the lower side of the Minor-damage relationship. The capacity relationships were calibrated directly to the individual threshold-exceedance observations using the Bayesian formulation presented in Section 3; the bin-averaged points are included only for graphical comparison and were not used in model fitting.

Table 1
Prior distributions adopted for the primary Bayesian capacity analysis and the prior sensitivity assessment.

Prior case	Prior for $\mu_{\ln C}$	Prior for $\sigma_{\ln C}$
Baseline	$\mu_{\ln C} \sim N(0, 10^2)$	$\sigma_{\ln C} \sim \text{Lognormal}(\ln 0.5, 1^2)$
Diffuse	$\mu_{\ln C} \sim N(0, 20^2)$	$\sigma_{\ln C} \sim \text{Lognormal}(\ln 0.5, 1.5^2)$
Moderately informative	$\mu_{\ln C} \sim N(-2, 5^2)$	$\sigma_{\ln C} \sim \text{Lognormal}(\ln 0.4, 0.5^2)$

The fitted empirical capacity curves represent the central probabilistic trends with their slopes reflecting the dispersion observed in the case-history data. Fig. 3 also includes the reference capacity curves reported by He and Rathje [11] (HR) for direct comparison. He and Rathje [11] fitted lognormal capacity relationships to bin-averaged exceedance probabilities using least-squares regression whereas the present study calibrates Bayesian threshold-exceedance models directly to the individual case-history observations. Therefore, the curves are not expected to be identical even though both use related case-history data and the same general lognormal capacity form. Fig. 3 additionally shows the deterministic RS limits proposed by Pells and Fell [9] (PF). For the Minor DS, the deterministic limit lies within the transition zone of the empirical curve approximately corresponding to the onset of Minor damage. For the Moderate and Severe DSs, the deterministic limits are near the lower-tail region of the empirical curves. Specifically, the PF thresholds of approximately 0.2% RS for Moderate damage and 1.0% RS for Severe damage lie below the corresponding median capacities, $RS_{50} = 0.472\%$ and $RS_{50} = 2.218\%$, respectively. Thus, nonzero exceedance probabilities are predicted at RS values close to and in some cases below these deterministic limits. Accordingly, the deterministic thresholds do not capture the gradual transitions and dispersion inherent in the probabilistic capacity relationships and may yield comparatively conservative criteria for Moderate and Severe damage.

The comparison with HR shows that the Moderate and Severe damage relationships are in close agreement with the published reference curves, with $RS_{50} = 0.472\%$ versus 0.460% for Moderate damage and $RS_{50} = 2.218\%$ versus 2.300% for Severe damage. For Minor damage, the median capacities are also of the same order 0.023% in the present model compared with 0.030% in HR. However, the present model exhibits a broader transition region because the Minor damage threshold is influenced by the overlap between DS1/no-damage and DS2/minor-damage observations at small relative crest settlements. This makes the onset of observable damage less sharply defined and leads the Bayesian calibration to estimate a larger dispersion for the Minor threshold.

4.2. Bayesian capacity models

Fig. 4 presents the prior and posterior marginal distributions along with joint posterior samples of the seismic capacity parameters for the Minor, Moderate, and Severe DSs. For all DSs, the posterior distributions of the logarithmic median capacity ($\mu_{\ln C}$) are much narrower than the priors. This narrowing indicates substantial data-driven updating and reduced posterior uncertainty in the estimated median deformation capacities. The posterior distributions of the dispersion parameter ($\sigma_{\ln C}$) are also more concentrated indicating reduced posterior uncertainty in the estimated dispersion parameter rather than a reduction in the underlying capacity dispersion. The joint posterior samples demonstrate dependence between $\mu_{\ln C}$ and $\sigma_{\ln C}$. The posterior correlation coefficients between $\mu_{\ln C}$ and $\sigma_{\ln C}$, computed from the pooled MCMC samples are −0.790 for Minor, +0.467 for Moderate, and +0.670 for Severe damage. The sign of the correlation is governed by which part of the capacity exceedance curve the case-history data constrain, and hence on which side of the median the binding observations lie. Formally, along the set of ($\mu_{\ln C}$, $\sigma_{\ln C}$) pairs that keep the capacity exceedance curve passing through an observation at exceedance probability (P_f), $\mu_{\ln C} = \ln RS - \Phi^{-1}(P_f)\cdot\sigma_{\ln C}$, so that $\partial\mu_{\ln C}/\partial\sigma_{\ln C} = -\Phi^{-1}(P_f)$; observations below the median ($P_f < 0.5$, $\Phi^{-1}(P_f) < 0$) therefore produce a positive $\mu_{\ln C}$–$\sigma_{\ln C}$ dependence, whereas observations above the median ($P_f > 0.5$, $\Phi^{-1}(P_f) > 0$) produce a negative one.

For the Minor DS, the negative correlation arises because the

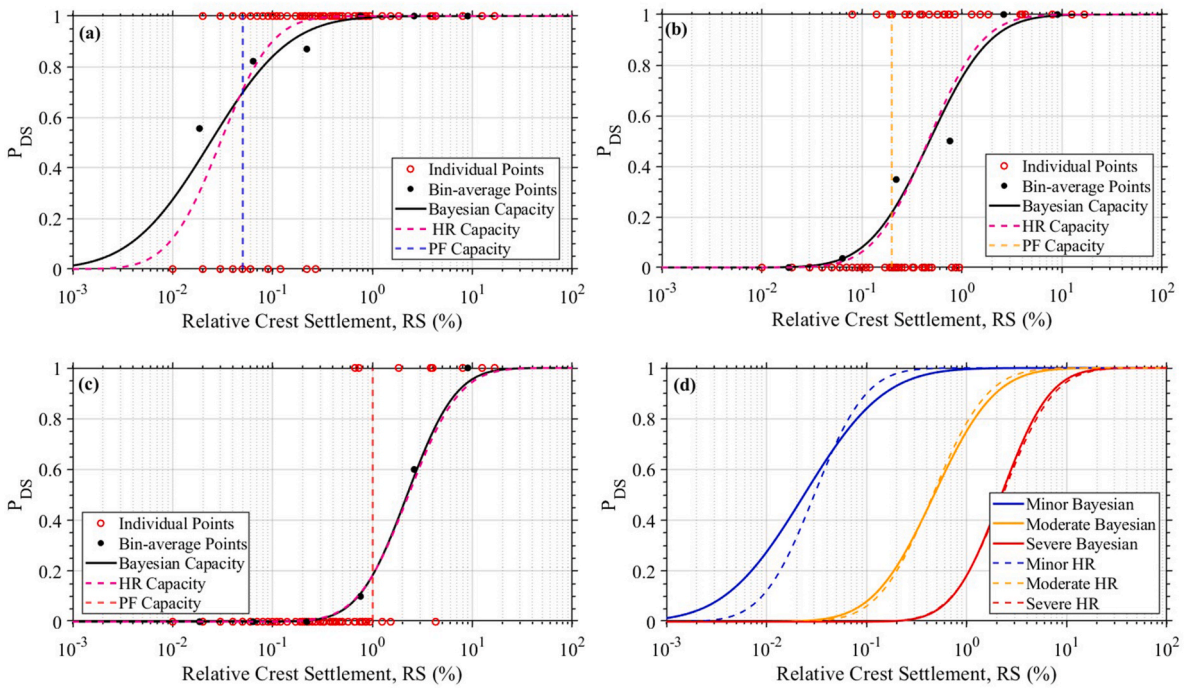


Fig. 3. Capacity relationships between relative crest settlement and damage-state exceedance probability for the: (a) Minor, (b) Moderate, and (c) Severe damage states, calibrated from the case-history database. Individual binary observations and bin-averaged exceedance probabilities are shown alongside the posterior median, together with the He and Rathje (HR) and Pells and Fell (PF) capacity models. (d) Comparison of the fitted Bayesian posterior-median capacity curves for all three damage states with the corresponding HR reference curves.

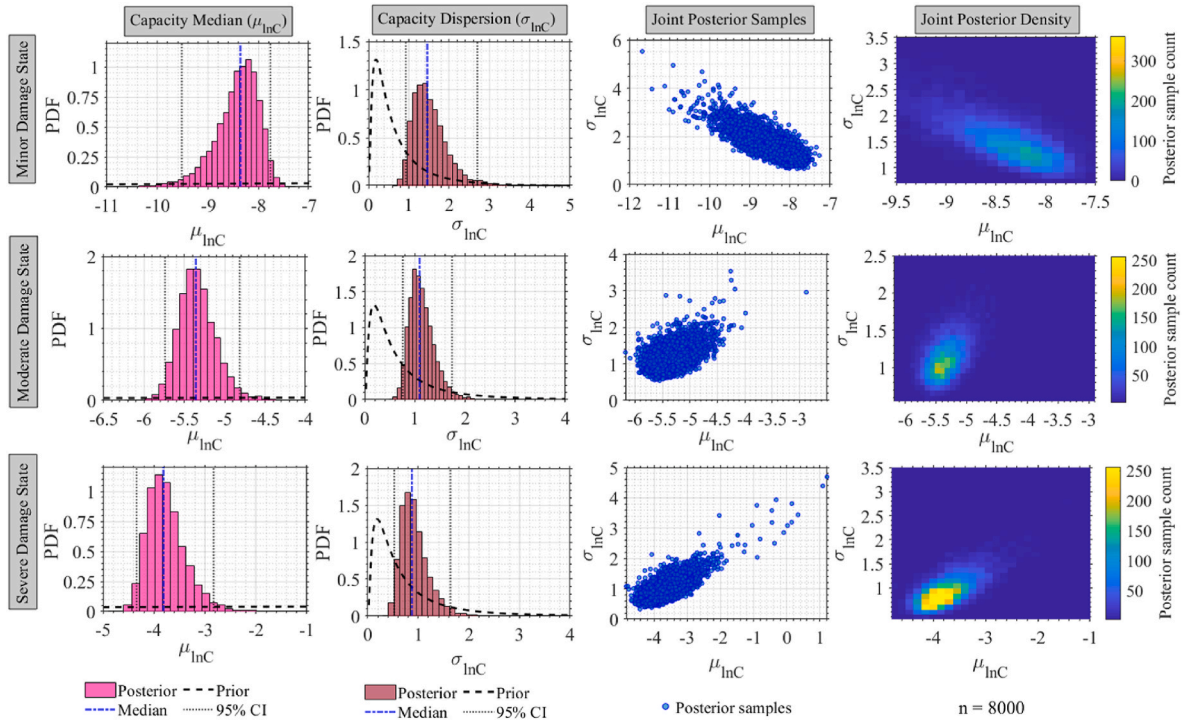


Fig. 4. Prior and posterior distributions of Bayesian seismic capacity parameters for the Minor, Moderate, and Severe damage states. For each damage state (rows), the left panels present the marginal posterior distribution of the logarithmic median capacity μ_{lnC} together with the corresponding prior, posterior median, and 95% credible interval, while the adjacent panels show the marginal posterior and prior distributions of the dispersion parameter σ_{lnC}. The right panels display 8000 retained MCMC posterior samples pooled across chains, along with the corresponding joint posterior density in the (μ_{lnC}, σ_{lnC}) space.

informative observations lie predominantly above the median. The Minor threshold is the lowest modeled damage threshold and is exceeded in most case histories, so the RS levels that constrain the fitted curve fall above the relatively small median capacity, in the high-exceedance region ($P_f > 0.5$). There, a higher median capacity requires a smaller dispersion, whereas a lower median capacity admits a larger dispersion, to preserve the observed exceedance pattern. Because the binding constraint lies above the median, μ_{lnC} and σ_{lnC} trade off in opposite directions, producing the negative posterior correlation.

For the Moderate and Severe DSs, the correlations are positive. These higher thresholds are exceeded in comparatively few case histories so their fitted medians fall toward the upper end of the observed RS range, and the observations that constrain the fitted curve lie predominantly below the respective median capacities in the low-exceedance region ($P_f < 0.5$). With few points constraining that region a larger median capacity (shifting the capacity exceedance curve toward higher RS) must be accompanied by greater dispersion for the curve to continue passing through the same sparse exceedance data; conversely, a smaller median capacity allows a smaller dispersion. Because the binding constraint lies below the median, μ_{lnC} and σ_{lnC} adjust in the same direction, producing the positive posterior correlations.

In summary, the μ_{lnC}–σ_{lnC} dependence reflects whether the available case-history data constrain each capacity exceedance curve on the high-exceedance side above the median for Minor damage, producing a negative correlation, or on the low-exceedance side below the median for Moderate and Severe damage, producing a positive correlation. These correlations are statistical posterior dependencies between fitted capacity parameters, not physical correlations between independent material properties. The lack of multimodality or boundary accumulation indicates stable and clearly defined parameter estimates.

Table 2 shows posterior parameter summaries as medians and 95% credible intervals. The median deformation capacity, which is the RS that corresponds to a 50% exceedance probability (RS_{50}), increases progressively with damage severity: approximately 0.023% for Minor damage, 0.47% for Moderate damage, and 2.22% for Severe damage. These values are consistent with the posterior median values of $\mu_{lnC} = -8.36$, -5.36, and -3.81 for Minor, Moderate, and Severe damage, respectively. As damage severity increases, the posterior median dispersion decreases from $\sigma_{lnC} = 1.45$ for Minor damage to 1.10 for Moderate damage and 0.87 for Severe damage. The larger dispersion for the Minor DS reflects the greater scatter associated with the onset of observable damage, where DS1/no-damage and DS2/minor-damage observations overlap at small RS values. DS1 records were retained as non-exceedance observations for the Minor damage threshold; therefore, the larger Minor dispersion is not due to omission of DS1 data. Instead, it reflects the gradual and less sharply defined transition from no damage to Minor damage in the case-history data. For Moderate and Severe damage, the exceedance transitions occur at larger RS values and are more clearly separated in the available observations, resulting in steeper capacity relationships and smaller posterior median dispersions. This trend concerns the fitted capacity dispersion governing the spread of the RS–DS relationship and does not imply that the Severe damage capacity parameters have lower posterior uncertainty. Indeed, because the number of high-damage observations is limited, the Severe DS has wider credible intervals for the capacity parameters.

Table 2
Posterior median Bayesian capacity parameters.

Damage State	μ_{lnC} (median [95% CI])	σ_{lnC} (median [95% CI])	RS_{50} (%) (median [95% CI])
Minor	−8.36 [−9.65, −7.78]	1.45 [0.93, 2.67]	0.023 [0.006, 0.042]
Moderate	−5.36 [−5.73, −4.83]	1.10 [0.75, 1.75]	0.47 [0.32, 0.80]
Severe	−3.81 [−4.36, −2.86]	0.87 [0.54, 1.58]	2.22 [1.28, 5.72]

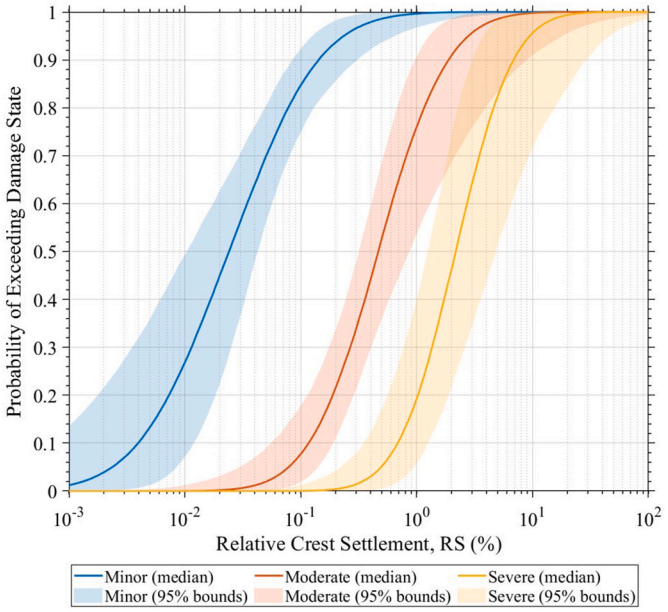


Fig. 5. Bayesian seismic capacity curves for Minor, Moderate, and Severe damage states expressed in terms of relative crest settlement, shown with posterior median estimates and 95% credible intervals.

Fig. 5 shows the Bayesian capacity curves with 95% credible intervals. The posterior median curves exhibit smooth sigmoidal transitions and preserve the expected DS ordering. The posterior median curves in Fig. 5 are derived from the same Bayesian capacity models represented by the central fitted relationships in Fig. 3d and therefore show closely corresponding transition locations. They also remain broadly consistent with the He and Rathje [11] reference curves, particularly for the Moderate and Severe DSs, while the Minor relationship exhibits a broader transition, as discussed in Section 4.1. The principal difference between the figures is their treatment of uncertainty: Fig. 3d compares the central fitted and reference capacity relationships, whereas Fig. 5 presents the posterior median curves together with 95% credible intervals obtained from the inferred capacity-parameter distributions. The widest intervals occur for the Minor DS because of scatter near the onset of observable damage and for the Severe DS because of the limited number of high-damage case histories, whereas the Moderate damage relationship is more tightly constrained.

4.3. Bayesian model diagnostics

Bayesian capacity parameters were estimated independently for each DS using an MCMC algorithm. As summarised in Table 3, four parallel chains were run for 25,000 iterations per DS, with the first 5000 discarded as burn-in. A thinning factor of 10 was applied to the post-burn-in samples used for posterior summaries and uncertainty estimation. ESS values were computed from the pooled unthinned post-burn-in chains thereby retaining the full set of available samples when evaluating sampling efficiency [50,51]. The posterior distributions in Fig. 4 are well defined and unimodal for all DSs, providing an initial qualitative indication of stable inference. Posterior uncertainty in σ_{lnC} varies across DSs, with comparatively greater uncertainty for the Severe DS because of the limited number of high-damage observations, as discussed in Section 4.2.

Convergence diagnostics are shown in Fig. 6. The concatenated post burn-in traces display stable fluctuations without systematic drift, and the ACFs decrease steadily with increasing lag, indicating adequate mixing. The Gelman–Rubin convergence diagnostic (split-$\widehat{R}$) is at or below 1.02 for both capacity parameters across all DSs (Table 3), well

Table 3
MCMC convergence and sampling diagnostics for Bayesian capacity models.

Damage State	No. of Chains	Iterations per Chain	Burn-in	Thinning	Acceptance Rate (mean [min–max])	Split-$\hat{R}$ (μ_{lnC})	Split-$\hat{R}$ (σ_{lnC})
Minor	4	25,000	5000	10	0.30 [0.28–0.32]	1.01	1.02
Moderate	4	25,000	5000	10	0.29 [0.27–0.31]	1.00	1.00
Severe	4	25,000	5000	10	0.31 [0.29–0.33]	1.01	1.02

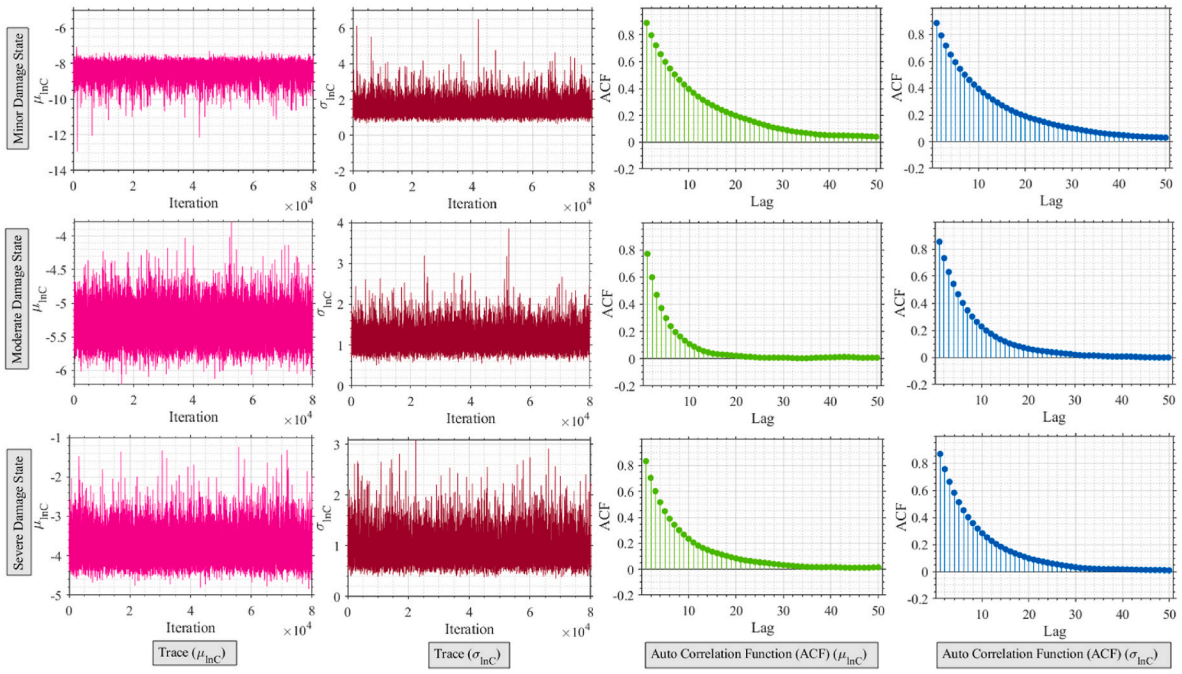


Fig. 6. Markov chain Monte Carlo (MCMC) convergence diagnostics for the Bayesian capacity model parameters across damage states. Rows correspond to the Minor, Moderate, and Severe damage states. For each damage state, trace plots of the posterior samples for the logarithmic median capacity, μ_{lnC}, and dispersion, σ_{lnC}, are shown in the first two columns, while the corresponding autocorrelation functions (ACFs) for μ_{lnC} and σ_{lnC} are shown in the third and fourth columns, respectively.

Table 4
Bayesian model diagnostics for damage state-specific capacity models.

Damage State Threshold	ESS (μ_{lnC})	ESS (σ_{lnC})	WAIC
Minor (k = 2)	3119	3228	63.02
Moderate (k = 3)	10086	5717	67.67
Severe (k = 4)	4915	4871	24.09

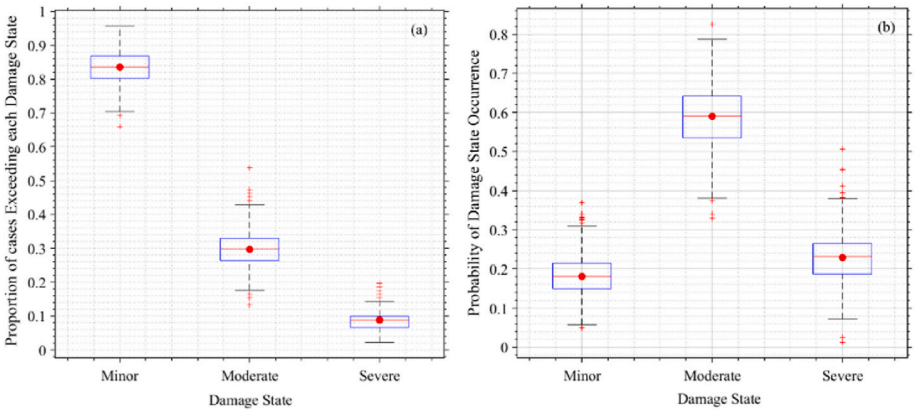


Fig. 7. Posterior predictive checks comparing observed and posterior predictive damage-state probabilities: (a) exceedance proportions and (b) mutually exclusive damage-state occurrence probabilities.

within the commonly adopted threshold of 1.05 and confirming convergence of the pooled chains. Short-lag autocorrelation is more evident for $\sigma_{\ln C}$, particularly for the Severe DS, but decreases at higher lags. Sampling efficiency and predictive adequacy are summarised in Table 4 using ESS and the WAIC. ESS values are in the thousands for all parameters, indicating adequate MCMC sampling efficiency. The highest ESS values are obtained for the Moderate DS, whereas the lower values for the Minor DS reflect greater posterior autocorrelation; nevertheless, the ESS values remain adequate for all DSs. The WAIC values provide DS-specific measures of predictive adequacy for the fitted capacity models. Because the models represent different threshold-exceedance outcomes, the WAIC values are reported diagnostically rather than used to rank the DS-specific models.

Fig. 7 displays posterior predictive performance for the DS exceedance proportions and the corresponding mutually exclusive DS-occurrence proportions. Panel (a) compares the observed and posterior predictive exceedance proportions for each DS threshold k. For posterior predictive replication r, these proportions are defined as:

$$\widehat{P}_{\geq k}^{obs} = \frac{1}{N}\sum_{i=1}^{N} y_i^{(k)} \;;\; \widehat{P}_{\geq k}^{rep,r} = \frac{1}{N}\sum_{i=1}^{N} y_i^{rep,(k,r)} \tag{9}$$

where N = 91 is the number of calibration records, $y_i^{(k)} = \mathrm{I}(DS_i \geq k)$ is the observed threshold-exceedance indicator, and the replicated indicator is generated as:

$$y_i^{rep,(k,r)} \sim Bernoulli\left(p_i^{(k,r)}\right)$$

with

$$p_i^{(k,r)} = \Phi\left(\frac{\ln(RS_i) - \mu_{\ln C,k}^{(r)}}{\sigma_{\ln C,k}^{(r)}}\right)$$

where $\mu_{\ln C,k}^{(r)}$ and $\sigma_{\ln C,k}^{(r)}$ are drawn jointly from the posterior distribution for threshold k. Each posterior draw produces one replicated binary dataset, and the boxplots summarise the resulting distribution of $\widehat{P}_{\geq k}^{rep,r}$ across 1000 posterior predictive replications.

Panel (b) presents dataset-level posterior predictive summaries of the mutually exclusive DS occurrence proportions. For each replication r, the threshold-specific replicated exceedance proportions were first converted into unnormalized occurrence proportions as:

$$\left.\begin{aligned} \widetilde{\pi}_1^r &= max\left(0, 1 - \widehat{P}_{\geq 2}^{rep,r}\right) \\ \widetilde{\pi}_2^r &= max\left(0, \widehat{P}_{\geq 2}^{rep,r} - \widehat{P}_{\geq 3}^{rep,r}\right) \\ \widetilde{\pi}_3^r &= max\left(0, \widehat{P}_{\geq 3}^{rep,r} - \widehat{P}_{\geq 4}^{rep,r}\right) \\ \widetilde{\pi}_4^r &= max\left(0, \widehat{P}_{\geq 4}^{rep,r}\right) \end{aligned}\right\} \tag{10}$$

where $\widetilde{\pi}_1^r, \widetilde{\pi}_2^r, \widetilde{\pi}_3^r, \widetilde{\pi}_4^r$ correspond to no damage, Minor damage, Moderate damage, and Severe damage respectively. Because the threshold-specific models were fitted independently, occasional violations of the required exceedance ordering can occur among posterior predictive replications. Negative adjacent differences were therefore truncated to zero, consistent with the implemented computational procedure. The resulting occurrence proportions were then normalized as:

$$\pi_j^r = \frac{\widetilde{\pi}_j^r}{\sum_{l=1}^{4} \widetilde{\pi}_l^r}, j = 1, \ldots, 4$$

The boxplots in Fig. 7b summarise the posterior predictive distributions of π_j^r, while the red markers show the observed DS occurrence proportions obtained from the corresponding observed threshold exceedance proportions.

4.4. Consistency between observed damage states and predicted probabilities

The relationship between observed damage classifications and Bayesian model predictions was examined by grouping predicted exceedance probabilities by observed damage state (Table 5). The predicted probabilities increase consistently with damage severity. The mean probability of exceeding the Minor damage threshold (DS ≥ 2) increases from 0.621 for no damage cases to 0.822, 0.958, and 0.995 for Minor, Moderate, and Severe damage cases respectively. Similarly, the mean probability of exceeding the Moderate damage threshold (DS ≥ 3) increases from 0.058 to 0.199, 0.494, and 0.882 across the same observed damage groups. The mean probability of exceeding the Severe damage threshold (DS ≥ 4) increases from 0.002 for no-damage cases to 0.019, 0.113, and 0.612 for Minor, Moderate, and Severe damage cases, respectively. This monotonic trend across all three calibrated thresholds indicates that cases with greater observed damage are assigned higher exceedance probabilities supporting the Bayesian capacity model's ability to preserve the observed ordering of damage severity. The comparatively high mean probability of Minor damage exceedance for the no damage group indicates limited separation between the no damage and Minor damage cases at the lowest threshold consistent with the substantial overlap in their observed RS values. Separation becomes progressively clearer for the higher damage thresholds.

Posterior predictive checks were performed by comparing observed DS exceedance proportions with replicated outcomes generated from the posterior models (Table 6). The observed exceedance proportions for DS ≥ 2, DS ≥ 3, and DS ≥ 4 were 0.835, 0.297, and 0.088, respectively. These observed proportions were closely reproduced by the corresponding posterior predictive medians and remained within the associated 95% posterior predictive intervals. The agreement between the observed and replicated damage proportions supports the consistency of the fitted Bayesian models with the empirical DS distribution. Because the same case-history dataset was used for model calibration, these results represent internal posterior predictive consistency checks rather than independent external validation. The diagnostics indicate that the Bayesian formulation preserves the observed damage trends while representing uncertainty in the RS–DS relationships.

Table 5
Predicted damage-state exceedance probabilities grouped by observed damage state.

Observed damage state	N	Mean predicted P(DS ≥ 2)	Mean predicted P(DS ≥ 3)	Mean predicted P(DS ≥ 4)
No damage (DS1)	15	0.621	0.058	0.002
Minor (DS2)	49	0.822	0.199	0.019
Moderate (DS3)	19	0.958	0.494	0.113
Severe (DS4)	8	0.995	0.882	0.612

Table 6
Posterior predictive checks for observed damage exceedance proportions.

Damage threshold	Observed proportion	Posterior predictive median	95% posterior predictive interval
DS ≥ 2 (Minor)	0.835	0.835	0.725–0.923
DS ≥ 3 (Moderate)	0.297	0.297	0.198–0.385
DS ≥ 4 (Severe)	0.088	0.088	0.033–0.143

Table 7
Prior sensitivity analysis results.

Prior	DS threshold	μ_{lnC} (median)	95% CI (low)	95% CI (high)	σ_{lnC} (median)	95% CI (low)	95% CI (high)
Baseline	Minor	−8.36	−9.52	−7.77	1.45	0.93	2.59
Baseline	Moderate	−5.35	−5.74	−4.79	1.10	0.75	1.77
Baseline	Severe	−3.80	−4.36	−2.85	0.88	0.53	1.59
Diffuse	Minor	−8.43	−9.89	−7.78	1.54	0.95	3.05
Diffuse	Moderate	−5.35	−5.73	−4.80	1.13	0.75	1.80
Diffuse	Severe	−3.79	−4.36	−2.76	0.90	0.53	1.70
Moderately	Minor	−8.15	−8.87	−7.69	1.17	0.82	1.82
Moderately	Moderate	−5.40	−5.75	−4.96	0.97	0.70	1.43
Moderately	Severe	−3.93	−4.39	−3.21	0.75	0.49	1.22

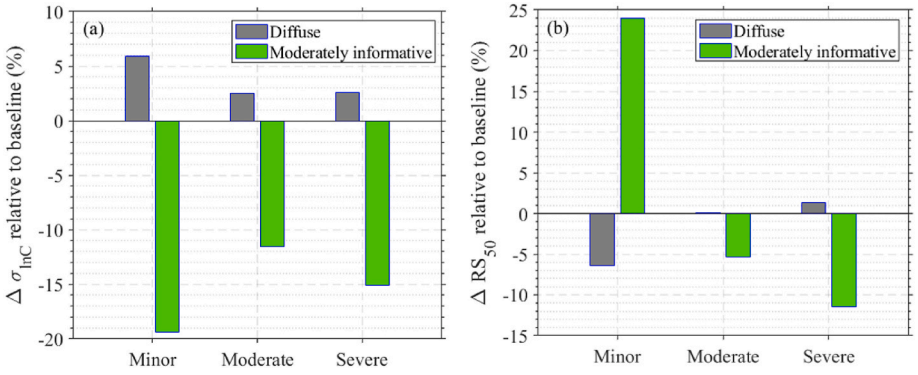


Fig. 8. Prior-sensitivity comparison expressed as percentage change relative to the Baseline prior: (a) posterior median capacity dispersion (σ_{lnC}), and (b) median capacity (RS_{50}). Positive values indicate an increase relative to the Baseline prior, and negative values indicate a decrease.

4.5. Prior sensitivity analysis

Table 7 summarises posterior medians and 95% credible intervals for the logarithmic median capacity μ_{lnC} and the dispersion parameter σ_{lnC}, obtained under Baseline, Diffuse, and Moderately informative prior specifications, for each DS threshold. Across all DSs, posterior estimates of μ_{lnC} are generally consistent among the prior specifications, with differences interpreted relative to their corresponding credible intervals. Substantial interval overlap is observed, indicating that estimates of median deformation capacity are primarily governed by the case-history data rather than by the prior assumptions. The resulting relative changes in RS_{50} and σ_{lnC} with respect to the Baseline prior are presented in Fig. 8. For positive-valued parameters, the relative change was calculated as:

$$\Delta X(\%) = \frac{X_{alternative\ prior} - X_{baseline\ prior}}{X_{baseline\ prior}} \times 100 \tag{11}$$

where X denotes either RS_{50} or σ_{lnC}. Because μ_{lnC} is a logarithmic parameter and may be negative, changes in μ_{lnC} were evaluated as absolute differences rather than ratios. The resulting relative changes are shown in Fig. 8. Under the Diffuse prior the changes in RS_{50} are approximately −6.4%, +0.1%, and +1.4% for Minor, Moderate, and Severe damage, respectively, and the corresponding changes in σ_{lnC} are approximately +5.9%, +2.5%, and +2.6%. Under the Moderately informative prior, the changes in RS_{50} are approximately +24.0%, −5.3%, and −11.5% for Minor, Moderate, and Severe damage, respectively, while σ_{lnC} changes by approximately −19.4%, −11.5%, and −15.1%.

Posterior estimates of the dispersion parameter σ_{lnC} display slightly greater sensitivity to prior specification, particularly for the Minor DS (DS ≥ 2), where the onset of observable damage is more weakly constrained by the available case-history data. However, variations in posterior median dispersion remain within the posterior uncertainty bounds shown in Table 7. Dispersion estimates for the Moderate and Severe DSs are comparatively stable across all prior specifications. The close agreement between the Baseline and Diffuse prior results indicates that the Baseline prior is weakly informative in practice for the available dataset. The larger changes obtained under the Moderately informative prior particularly for the Minor-damage model, demonstrate that stronger prior information can influence parameters that are less tightly constrained by the case-history data. Nevertheless, the substantial overlap among the posterior credible intervals indicates that the principal capacity trends and DS ordering remain robust. These findings support the use of the inferred deformation-based seismic capacity relationships in the subsequent fragility and risk analyses indicating that the resulting predictions are not unduly influenced by the choice of prior.

5. Application of Bayesian capacity models to fragility analysis and risk metrics

The Bayesian seismic capacity models developed in Section 3 are combined with probabilistic seismic demand models (PSDMs) to construct fragility curves that explicitly account for seismic demand variability, capacity dispersion, and posterior uncertainty in the inferred capacity parameters. This formulation provides a transparent and internally consistent basis for deformation-based seismic fragility and risk assessment. Fig. 9 presents a schematic overview of the proposed methodology, illustrating the integration of Bayesian capacity inference into the fragility analysis framework and risk analysis.

5.1. Application to fragility analysis

5.1.1. Seismic demand modeling

In seismic fragility assessment, earthquake loading is commonly represented using ground-motion IMs, while system response is quantified through an EDP. In this study, RS is adopted as the EDP. The relationship between IM and RS is described using a log-linear PSDM, which has been widely employed in deformation-based fragility analyses [10], [13]:

$$\ln EDP = \ln a + b \ln IM + \varepsilon \tag{12}$$

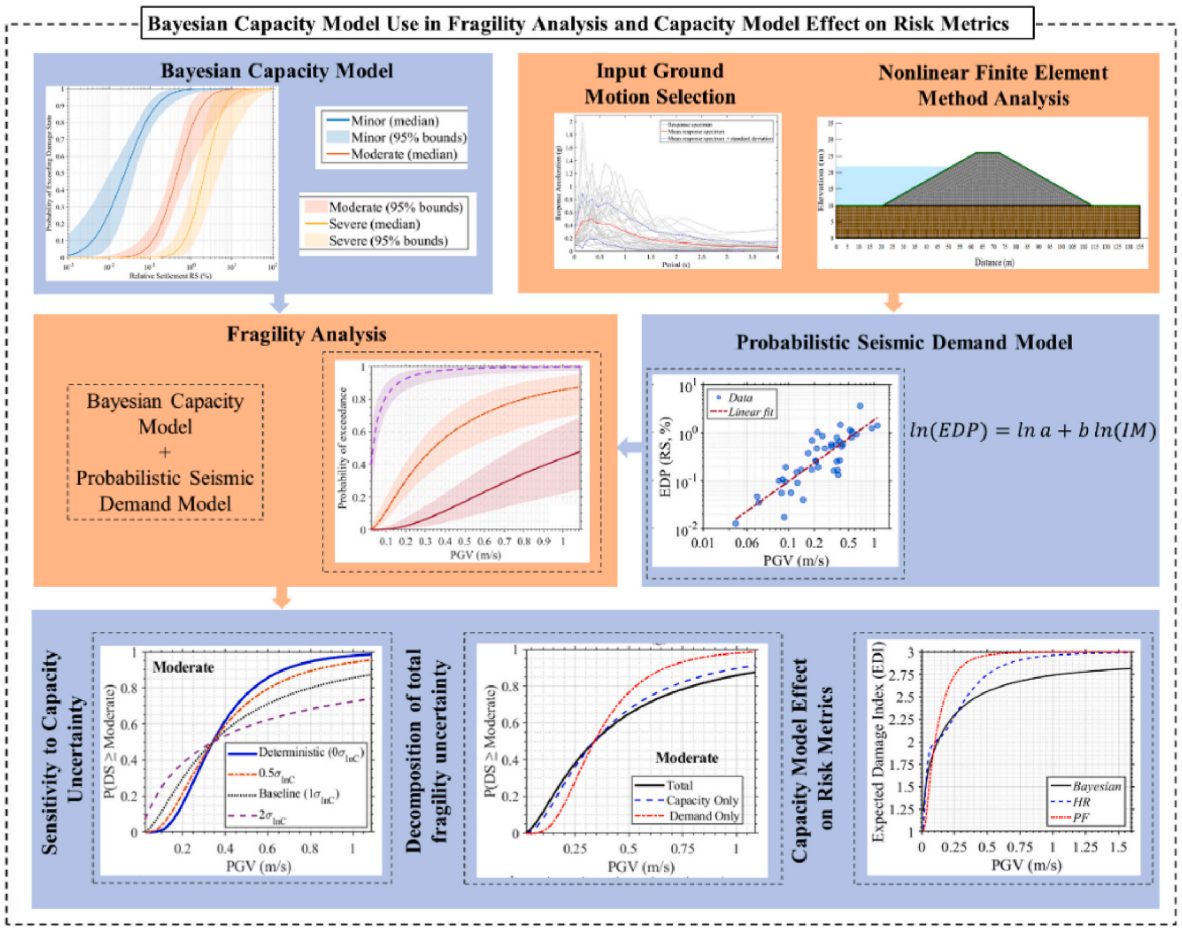


Fig. 9. Schematic illustrating the application of the proposed Bayesian probabilistic seismic capacity modeling framework to fragility analysis.

where a and b are regression coefficients describing the scaling of EDP with the selected IM, and ε is a zero-mean normally distributed residual term, $\varepsilon \sim N(0, \sigma^2_{\ln D})$ [52]. The residual dispersion $\sigma_{\ln D}$ represents variability in seismic demand not captured by the IM and constitutes the demand uncertainty in subsequent fragility calculations.

The regression parameters are estimated using ordinary least squares in logarithmic space. The residual standard deviation $\sigma_{\ln D}$ represents the dispersion of seismic demand about the median PSDM prediction and is subsequently incorporated into the fragility calculations. The median predicted RS for a given IM is expressed as:

$$\widehat{RS}(IM) = aIM^b \tag{13}$$

where $\widehat{RS}(IM)$ denotes the median EDP predicted by the PSDM, and $\sigma_{\ln D}$ characterizes the dispersion of RS about this median prediction.

5.1.2. Fragility curve development

Fragility curves describe the probability that a system exceeds a specified DS as a function of seismic IM [11,17]. In this study, fragility relationships are derived by analytically combining the PSDM described in Section 5.1.1 with the Bayesian seismic capacity models presented in Section 3. Assuming statistical independence between demand and capacity uncertainties, the probability of exceeding k^{th} DS conditional on IM can be expressed as:

$$P(DS \geq k|\, IM) = \Phi\left(\frac{\ln \widehat{RS}(IM) - \mu_{\ln C,k}}{\sqrt{\sigma^2_{\ln C,k} + \sigma^2_{\ln D}}}\right) \tag{14}$$

where $\ln \widehat{RS}(IM) = \ln a + b \ln IM$ denotes the median demand predicted by the PSDM, $\Phi(\cdot)$ is the standard normal cumulative distribution function, $\mu_{\ln C,k}$ and $\sigma_{\ln C,k}$ are the logarithmic median and dispersion of the RS capacity for k^{th} DS and $\sigma_{\ln D}$ is the lognormal standard deviation representing demand variability [18,32]. The combined dispersion in Eq. (14) arises from the convolution of lognormal demand and capacity distributions in logarithmic space. The PSDM thereby transforms the EDP-space capacity model into an IM-based fragility function. For numerical implementation, the fragility relationship is commonly expressed directly in IM space by defining the log-median IM associated with a 50% probability of exceeding k^{th} DS as:

$$\mu_{IM,k} = \frac{\mu_{\ln C,k} - \ln a}{b} \tag{15}$$

where $\mu_{IM,k}$ is the log-median IM at which the k^{th} DS has a 50% probability of exceedance.

$$\beta_{IM,k} = \frac{\sqrt{\sigma^2_{\ln C,k} + \sigma^2_{\ln D}}}{b} \tag{16}$$

where $\beta_{IM,k}$ is the total logarithmic dispersion of the fragility curve in IM space. The resulting fragility function can be written in the standard lognormal form:

$$P(DS \geq k|\, IM) = \Phi\left(\frac{\ln IM - \mu_{IM,k}}{\beta_{IM,k}}\right) \tag{17}$$

This formulation is consistent with established probabilistic fragility frameworks, including the methodology of He and Rathje [11], in which seismic capacity is represented using continuous DS exceedance

relationships with fixed median and dispersion parameters inferred from empirical data. In contrast, deterministic fragility approaches based on fixed Pells and Fell [9] thresholds neglect capacity dispersion entirely by setting $\sigma_{\ln C,k} = 0$. The Bayesian framework adopted here generalises these formulations by treating the capacity parameters $\mu_{\ln C,k}$ and $\sigma_{\ln C,k}$ as random variables inferred probabilistically from case-history data rather than as fixed point estimates.

Fragility curves are therefore obtained by propagating posterior samples of the capacity parameters through the demand-capacity formulation. For each posterior draw ($\mu^{(s)}_{\ln C,k}$, $\sigma^{(s)}_{\ln C,k}$), the DS exceedance relationship is first defined in EDP space as:

$$P^{(s)}(DS \geq k|RS) = \Phi\left(\frac{ln(RS) - \mu^{(s)}_{ln\ C,k}}{\sigma^{(s)}_{ln\ C,k}}\right) \tag{18}$$

where RS is the relative crest settlement taken as EDP. This EDP-space relationship is then mapped to IM space using the PSDM described in Section 5.1.1. For each posterior draw, the corresponding IM-space parameters $\mu^{(s)}_{IM,k}$ and $\beta^{(s)}_{IM,k}$ are computed using Eqs. (15) and (16), and a conditional fragility curve is obtained as:

$$P^{(s)}(DS \geq k|IM) = \Phi\left(\frac{\ln(IM) - \mu^{(s)}_{IM,k}}{\beta^{(s)}_{IM,k}}\right) \tag{19}$$

The ensemble of sampled IM-space fragility curves defines the posterior distribution of fragility. Median fragility curves and 95% credible intervals are obtained by summarizing the distribution of fragility across posterior samples at each IM value, thereby explicitly propagating posterior uncertainty in the capacity parameters into IM-based fragility estimates. The detailed derivation of the EDP space to IM space transformation is provided in Appendix A. The median fragility point (IM_{50}) corresponds to the IM at which the probability of exceeding DS_k equals 0.5. The total dispersion governing the shape of the fragility curve is given by:

$$\sigma^2_{total} = \sigma^2_{\ln C,k} + \sigma^2_{\ln D} \tag{20}$$

where σ_{total} denotes the total fragility dispersion, $\sigma_{\ln C,k}$ is the logarithmic capacity-dispersion parameter controlling the spread of the DS-specific capacity relationship, and σ_{lnD} represents demand uncertainty associated with record-to-record variability not captured by the selected IM. This additive decomposition provides a transparent means of assessing the relative contributions of capacity and demand uncertainty to the total fragility dispersion. Posterior uncertainty in $\mu_{lnC,k}$ and $\sigma_{lnC,k}$ is propagated separately through the posterior-sampling procedure defined in Eqs. (18) and (19).

5.2. Effect of capacity model choice on risk-based metrics

This section evaluates the effect of seismic capacity modeling assumptions on risk-informed performance measures. To enable a consistent and interpretable comparison across alternative capacity models, the fragility curves developed in Section 5.1 are transformed into a scalar risk metric, namely the Expected Damage Index (EDI). Damage-based indices of this type are widely employed in seismic risk assessment to aggregate DS exceedance probabilities into a single performance indicator suitable for comparative evaluation [53,54]. The effect of capacity model choice is examined by comparing risk estimates obtained using three alternative seismic capacity formulations: (1) the Bayesian seismic capacity model developed in this study, (2) a non-Bayesian probabilistic capacity model consistent with the HR formulation, and (3) a deterministic capacity model based on fixed PF deformation thresholds.

For a given IM level, DS exceedance probabilities derived from the fragility curves are first converted into mutually exclusive DS occurrence probabilities through probability differencing. These probabilities represent the likelihood that the system occupies a specific DS at the specified seismic intensity. The EDI is then defined as:

$$EDI\ (IM) = \sum_k w_k P(DS = k|IM) \tag{21}$$

where the probability of occurrence of damage state k is given by:

$$P(DS = k|IM) = P(DS \geq k|IM) - P(DS \geq k+1|IM) \tag{22}$$

where $P(DS = k|IM)$ denotes the probability that the system is in damage state k at the specified IM, and w_k is a weighting factor reflecting the relative severity of that DS. For the highest modeled state, Severe damage, $P(DS = Severe|IM) = P(DS \geq Severe|IM)$, because no higher damage threshold is included in the present analysis. In this study, ordinal integer weights are assigned in increasing order of damage severity, with w = 1, 2, and 3 corresponding to Minor, Moderate, and Severe DSs, respectively (with an implicit weight of 0 for the No damage state). Such ordinal weighting schemes are commonly adopted when expected damage indices are used for comparative or diagnostic purposes rather than as direct estimators of economic loss or repair cost, and they allow the relative influence of different capacity modeling assumptions on risk estimates to be systematically evaluated [53,54]. With these weights, the EDI is bounded between 0 and 3 and admits a direct interpretation on the adopted ordinal damage scale. Substituting Eq. (22) into Eq. (21) shows that the occurrence-weighted definition is algebraically equivalent to the sum of the three damage-state exceedance probabilities, $EDI\ (IM) = P(DS \geq Minor|IM) + P(DS \geq Moderate|IM) + P(DS \geq Severe|IM)$, which is the cumulative form used in the computation. For the Bayesian formulation, the EDI is evaluated for each posterior sample by summing the corresponding sampled Minor, Moderate, and Severe damage exceedance probabilities at each IM value. The resulting ensemble of sampled EDI curves defines the posterior EDI distribution, from which the posterior median and 95% credible interval are obtained. The paired posterior capacity-parameter samples are retained during this calculation to preserve their inferred dependence. In contrast, the HR and PF formulations use fixed capacity parameters and therefore produce single EDI curves without credible intervals.

The EDI is interpreted as follows. EDI = 0 corresponds to the lower bound, in which the system is with probability one in the No-damage state, so no deformation-based damage is expected at the specified IM level. EDI = 3 corresponds to the theoretical upper bound, at which the system is, with probability one, in the Severe DS, the highest DS considered in this study; because Severe carries the maximum weight of 3, this represents the most adverse outcome on the adopted scale. Intermediate values represent the probability-weighted expected damage severity: when the probability distribution is concentrated in a single damage state, EDI = 1 and EDI = 2 correspond to the Minor and Moderate states, respectively; more generally, these values may also result from probabilistic mixtures of different DSs, while non-integer values, such as EDI = 1.6, indicate an expected severity lying between two states, reflecting a probabilistic mixture of damage outcomes at the given IM. Equivalently, in its cumulative form, the EDI may be read as the expected number of damage thresholds exceeded at the specified intensity. Because the index is based on an ordinal weighting scheme, it is intended as a relative comparative measure of expected damage severity across capacity models rather than a direct estimate of physical loss or repair cost; its absolute value is therefore most meaningfully interpreted within the adopted 0–3 scale and through comparison among the Bayesian, HR, and PF formulations.

6. Case study application

6.1. Embankment dam description

To demonstrate the application of the proposed Bayesian capacity

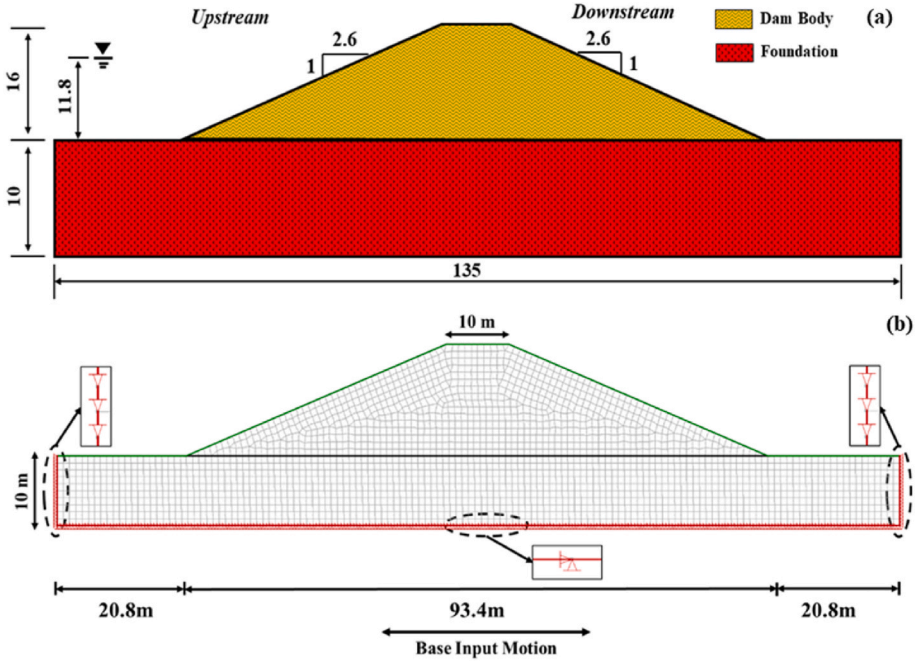


Fig. 10. (a) Cross-sectional configuration of the embankment dam adopted from Guo et al. [55], showing the dam body, foundation, slope geometry, and principal dimensions; (b) corresponding numerical model representation, including mesh discretization, boundary conditions, and applied base input motion.

Table 8
Soil parameters for the studied embankment dam (After Guo et al. [55]).

Dam Components	Properties			
	Effective Cohesion (kPa)	Effective friction angle (°)	Unit weight (kN/m^3)	Poisson's Ratio (ν)
Dam Body	8.9	34.8	20	0.3
Foundation	100	34.1	18	0.25

modeling framework in a seismic fragility and risk assessment context a benchmark embankment dam originally reported by Guo et al. [55] is analyzed. The dam is 16 m high, with upstream and downstream slopes of 1:2.6. The cross-section comprises the embankment body and the underlying foundation layer as shown in Fig. 10a. Material properties for both components are taken from Guo et al. [55] and summarised in Table 8. These include unit weight, effective cohesion, effective friction angle, and Poisson's ratio, together with the stress-dependent stiffness functions described in Section 6.3.2. This benchmark provides a reproducible and transparent basis for the illustrative demand analysis and is not intended to represent a uniquely critical dam height.

6.2. Seismic ground-motion selection

A suite of earthquake acceleration time histories was assembled from recordings at multiple stations. In the absence of a site-specific seismic hazard analysis for the dam location, input ground motions were selected from a COSMOS strong motion center database using a minimum PGA threshold of approximately 0.05 g. This criterion was adopted to retain motions that could induce nonlinear response and measurable deformation in the embankment dam. The selected records span an M_w range from 4.8 to 7.6. Horizontal components of the ground motions were applied at the base of the model. In total, thirty-seven free-field records from thirteen earthquakes were used, supplemented by seven additional records obtained from six instrumented embankment dam sites, giving forty-four input ground-motion records. A summary of the selected ground motions is provided in Table 9; the complete record-level metadata, including recording station, station type and location, available measured Vs30, moment magnitude, hypocentral distance, focal depth, and the computed intensity measures (PGA, PGV, and VRMS), are provided in the Supplementary File 1 (Table S1), while their magnitude–distance distribution and response spectra are illustrated in Fig. 11. The definitions of PGA, PGV, and VRMS, including calculation of VRMS over the full processed record duration, are provided in Appendix B.

6.3. Numerical model and dynamic analysis

6.3.1. Finite-element model and analysis stages

A two-dimensional finite element model of the benchmark embankment dam described in Section 6.1 was developed in QUAKE/W [56] for nonlinear dynamic analyses under plane-strain conditions. The embankment and foundation were assigned silty sand and altered schist properties, respectively [57], using the material parameters summarised in Table 8. Mesh discretization followed the seismic wave-propagation criterion requiring element size smaller than one-eighth to one-tenth of the wavelength at the highest excitation frequency [58]. A uniform mesh size of 1 m was adopted (Fig. 10b). The dam and foundation were modeled as deformable continua within a single finite element mesh to capture dam–foundation interaction, deformation compatibility, and stress transfer [59]. This modeling approach is consistent with QUAKE/W simulation procedures [56] and previous studies [10,14,55,60]. The analysis was performed in two stages. In the static stage, geostatic equilibrium and the initial effective-stress state were established under gravity loading with hydrostatic pore-water pressures corresponding to a reservoir level of 11.8 m as determined by a defined phreatic line [55]; the negligible residual forces and displacements observed at the end of this stage confirmed satisfactory static equilibrium. In the dynamic stage, the initial pore-water-pressure distribution was retained while transient seepage and cyclic excess pore-water-pressure generation were not modeled. The dynamic response was evaluated using a nonlinear stress–deformation formulation initialized from the static effective-stress state; the associated assumptions are discussed in Section 6.3.5.2.

Table 9
Summary of Earthquakes used in the analysis.

Station Location	Earthquake	Date	M_w	D_f (km)	No. of Records
Free Field	Chichi	1999/09/20	7.6	8	9
	Kobe	1995/01/16	6.9	17.6	13
	Imperial	1979/10/15	6.9	10	1
	Kozani-Grevena	1995/05/15	5.1	14	2
	Loma Prieta	1989/10/17	6.9	18	3
	Manjil-Rudbar	1990/06/20	7.4	15	1
	Westmorland	1981/04/26	5.9	10	2
	Friuli	1976/05/06	6.4	10	1
	Hollister	1961/04/09	4.8	-	1
	Kocaeli	1999/08/17	7.4	17	1
	Landers	1992/06/28	7.3	10	1
	Northridge	1994/01/17	6.7	17.5	1
	Trinidad	1983/08/24	6.1	-	1
Anderson Dam	Morgan Hills	1984/04/24	6.2	8	1
	Loma Prieta	1989/10/18	6.9	18	1
Carbon Canyon Dam	Northridge	1994/01/17	6.7	17.5	1
Long Valley Dam	Chalfant Valley	1986/07/21	6.4	19	1
Prado Dam	Northridge	1994/01/17	6.7	17.5	1
Santa Felica Dam	Northridge	1994/01/17	6.7	17.5	1
Tolt River Dam	Duval	1996/05/03	5.3	7	1

Abbreviations: M_w: Moment Magnitude, D_f: Focal Depth.

6.3.2. *Constitutive model and stress-dependent stiffness*

Nonlinear soil behavior was represented using the QUAKE/W Nonlinear material model comprising a hyperbolic stress–strain backbone with Masing-type unloading and reloading rules [5,56]. This model captures strain-dependent shear-stiffness reduction and hysteretic energy dissipation, which are important for representing the response of embankment materials under strong ground motion [61]. The symmetric hyperbolic backbone is expressed as:

$$\tau(\gamma) = \frac{G_{max}\gamma}{1 + \frac{|\gamma|}{\gamma_{ref}}} \tag{23}$$

where τ is the shear stress, γ is the shear strain, G_{max} is the small-strain shear modulus, and $\gamma_{ref} = \tau_{max}/G_{max}$ is the reference shear strain governing the curvature of the backbone, with τ_{max} being the confinement-dependent shear strength obtained from the Mohr–Coulomb parameters (c', ϕ') listed in Table 8. The resulting γ_{ref} values range from approximately 10^{-4} to 10^{-3} and are consistent with low-plasticity silty soils [62]. The corresponding secant shear modulus decreases progressively with increasing strain and reaches $0.5G_{max}$ at $|\gamma| = \gamma_{ref}$ [61]. Fig. 12 schematically illustrates the adopted backbone and cyclic unloading–reloading response: the initial slope is defined by G_{max}, the large-strain asymptotes by the confinement-dependent shear strength, and the enclosed loop area represents hysteretic energy dissipation. The figure is conceptual rather than extracted from the finite-element analysis, and a similar schematic has been used in a nonlinear QUAKE/W analysis of an earth dam [63].

The small-strain shear modulus (G_{max}) was defined in QUAKE/W using Hardin-type relationships that account for the effect of confining stress on stiffness [64]. Different formulations were used for the dam body and foundation. For the dam body, a cohesive-soil formulation was adopted with small-strain stiffness expressed in terms of void ratio and

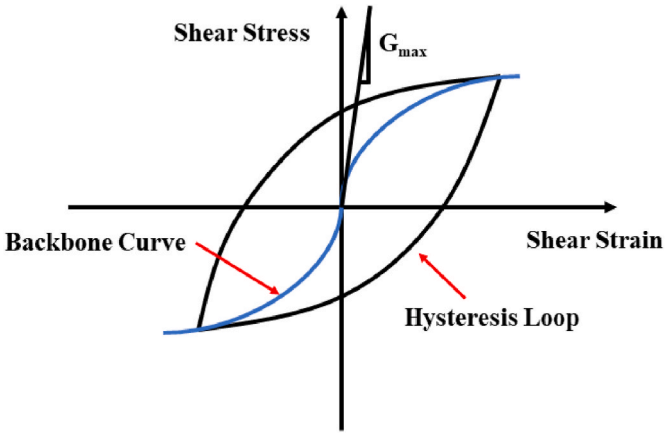


Fig. 12. Conceptual schematic of the hyperbolic backbone and Masing-type cyclic unloading–reloading response used to describe the nonlinear material formulation. The initial backbone slope represents G_{max}, and the area enclosed by the cyclic loop represents hysteretic energy dissipation. The figure is illustrative and does not represent a stress–strain loop extracted from the finite-element analysis.

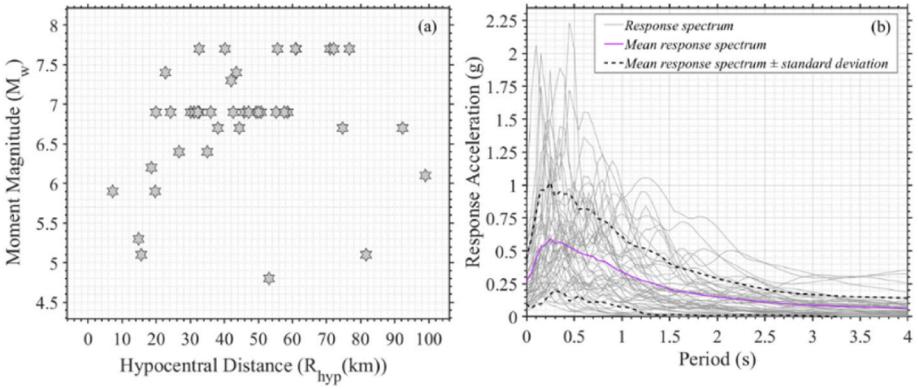


Fig. 11. Characteristics of the selected ground motions: (a) distribution of moment magnitude as a function of hypocentral distance; (b) response acceleration spectra of individual records, together with the mean spectrum and mean ± standard deviation.

local mean effective stress [65–67]. The stress-dependent G_{max} function was generated from the over consolidation ratio (OCR), void ratio (e), plasticity index (PI), and local mean effective stress (σ'_m), with the coefficient of earth pressure at rest (K_0) used to establish the initial lateral stress state; a PI of 10, an OCR of 1, and e = 0.5 were adopted. The formulation for G_{max} follows:

$$G_{max} = 625\left(\frac{1}{0.3+0.7e^2}\right)(OCR)^m\sqrt{P_a\sigma'_m} \quad (24)$$

where σ'_m is the mean effective stress and P_a is atmospheric pressure. In this formulation, the stress exponent is a constant 0.5 while the influence of plasticity is captured by the exponent m, which is defined as $m = PI^{0.72}/50$. For the foundation, a granular-soil formulation employing a dense, rock-like analogue was adopted to represent the fractured schist, consistent with its pressure-dependent stiffness behavior [66,68]. In this formulation, the stiffness coefficient (K), an empirical parameter related to relative density and grain characteristics, governs the material stiffness. A value of K = 180 was adopted to represent the comparatively high stiffness of the altered schist [68]. The corresponding expression for G_{max} is:

$$G_{max} = 22K\sqrt{P_a\sigma'_m} \quad (25)$$

Eqs. (24) and (25) were used to generate stress-dependent G_{max} data points over the specified stress range, and the local G_{max} was evaluated from the local effective-stress state [56]. The resulting G_{max} values increase with effective confinement, ranging from approximately 41.5–191.5 MPa for the dam body and 97.5–455.9 MPa for the foundation (Fig. 13). The corresponding small-strain shear-wave velocities were not prescribed directly in QUAKE/W but were derived from the G_{max} values as $V_{s,max} = \sqrt{G_{max}/\rho}$, where ρ is the mass density, and range from approximately 143–306 m/s for the dam body and 231–499 m/s for the foundation.

6.3.3. Damping formulation

Energy dissipation in the adopted nonlinear formulation was represented by two complementary mechanisms: material hysteresis generated by the nonlinear constitutive response and supplementary viscous damping introduced through the global Rayleigh damping matrix. As described in Section 6.3.2, the hysteretic component is generated naturally by the hyperbolic stress–strain backbone and Masing-type unloading–reloading rules; under cyclic loading these rules form stress–strain loops whose enclosed area represents the energy dissipated through material hysteresis (Fig. 12). At very small strain levels, however, the hysteretic loop area approaches zero, and supplementary viscous damping is therefore incorporated in nonlinear time-domain analyses [69]. In QUAKE/W this contribution is introduced through the Rayleigh damping matrix $[D] = \alpha[M] + \beta[K]$, where [D], [M], and [K] are the damping, mass, and stiffness matrices, respectively, and the coefficients α and β are determined from the specified damping ratio and the lowest and second-lowest system frequencies [56]. The supplementary viscous damping ratio (ξ_v) was represented as:

$$\xi_v = \xi_{max}\left(1 - \frac{G}{G_{max}}\right) \quad (26)$$

where G is the shear modulus obtained from the same effective-stress dependent material function evaluated at the current effective stress, G_{max} is the stress-dependent small-strain shear modulus, and ξ_{max} is the user-defined maximum damping ratio. When $G = G_{max}$, or when Eq. (26) gives a value below the specified minimum, the minimum damping ratio governs [56].

In this study, a minimum damping ratio of 0.05 was assigned to both materials, with maximum values of $\xi_{max} = 0.35$ for the dam body and 0.15 for the foundation. The adopted damping ratios for the embankment are consistent with those used in a published nonlinear QUAKE/W analysis of an earth dam by Hu et al. [63]. No separate target damping curve was prescribed. Because cyclic excess pore-water-pressure generation was not modeled, changes in G and supplementary damping due to pore-pressure-induced effective-stress reduction were not represented. Eq. (26) therefore defines only the supplementary viscous component, whereas hysteretic dissipation arises from the cyclic stress–strain response illustrated in Fig. 12.

6.3.4. Time integration, convergence, and boundary conditions

Each ground-motion analysis followed the two-stage procedure described in Section 6.3.1. During the static stage, horizontal displacements were fixed along the lateral boundaries, and the base was restrained in both directions to establish the initial stress state. For the subsequent dynamic stage, vertical displacements were constrained along the lateral boundaries to permit horizontal deformation, the base remained fully restrained, and the acceleration time history was prescribed as the seismic input. The nonlinear equations of motion were integrated in the time domain using the Wilson-θ method in which the acceleration is assumed to vary linearly over the extended interval t to $t + \theta\Delta t$ (with $\theta \geq 1.0$) and the response quantities are advanced sequentially at each time step [56]. Each processed accelerogram was analyzed over its full duration with the integration time increment set no greater than the sampling interval of the input motion in accordance with QUAKE/W guidance [56]. For a representative record (PGA = 0.251 g; Supplementary File 1, Table S1), the processed duration of approximately 34.17 s was discretized into 4093 time steps of approximately 0.00835 s. Convergence at each time step was controlled by a maximum of 10 iterations, a displacement-difference tolerance of 5×10^{-4} m, and a convergence criterion of three significant digits.

In QUAKE/W, boundaries are represented through displacement or force constraints, and dedicated non-reflecting (absorbing or free-field)

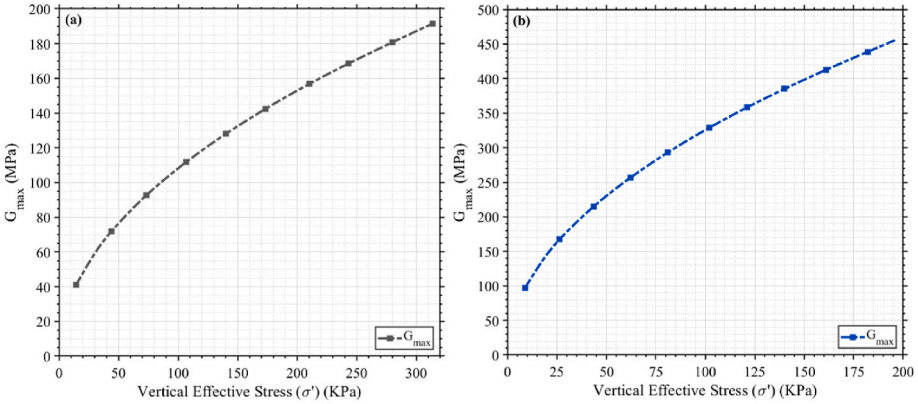


Fig. 13. Variation of small-strain shear modulus (G_{max}) with vertical effective stress (σ'_v): (a) Dam body and (b) Foundation.

boundary formulations are not provided; the computed motion is therefore relative to the restrained base, and the reported crest settlements represent deformation of the dam–foundation system rather than absolute motion [56]. The foundation domain spans a total width of 135 m (approximately 8.4H for the 16 m high dam), including lateral extensions of approximately 20.8 m (1.3H) on each side of the embankment, which place the lateral boundaries outside the embankment footprint and away from the principal deformation region. This configuration is consistent with the QUAKE/W modeling framework [56], the published reference model adopted in this study [55], and related seismic analyses of slopes and embankment dams using QUAKE/W [60,63,70,71].

6.3.5. Numerical assumptions and limitations

The main modeling assumptions that condition the interpretation of the demand and fragility estimates, along with numerical stability considerations, are discussed below.

6.3.5.1. Boundary-effect qualification. The adopted model did not incorporate explicit free-field, transmitting, or absorbing boundaries; therefore, artificial reflections of seismic waves at the model boundaries cannot be entirely excluded [5,58,72,73]. The extent of any such effect depends on the domain dimensions, material stiffness, damping characteristics, and the frequency content of the input motion [5,74]. Accordingly, the adopted model is not intended to demonstrate complete independence from boundary effects.

A lateral-domain sensitivity analysis was conducted to quantify the influence of the lateral extent of the foundation on the computed seismic demand. A representative strong-motion analysis (PGA $\approx$ 0.329 g) was repeated using lateral foundation extensions of 20.8, 32, 48, and 64 m on each side of the embankment, corresponding to approximately 1.3H, 2H, 3H, and 4H, respectively. The crest settlement was evaluated at the end of the shaking phase for each model. Relative to the adopted 20.8 m extension, the 32, 48, and 64 m cases differed by approximately 0.1%, 1.4%, and 1.1%, respectively, indicating close agreement among the four domain widths and limited sensitivity of the crest-settlement demand to the tested lateral extent for this representative motion. These results do not, however, demonstrate complete boundary independence or the absence of reflected waves.

The spatial extent of the deformation pattern was further examined using the final post-shaking XY shear-strain contour from a separate representative ground-motion analysis with PGA $\approx$ 0.194 g (Supplementary File 2, Section S4 and Fig. S4). The contour shows localized shear-strain concentrations within the embankment body, while the strain magnitude decreases markedly through the lateral foundation extensions to near-background levels of approximately -5×10^{-5} to 5×10^{-5} in the outer foundation regions. No continuous wedge-shaped shear-strain band, failure surface, or localized shear-deformation zone extends from the embankment to either lateral boundary at $x = 0$ or $x = 135$ m. Although the final post-shaking contour cannot capture possible transient strain localization during earlier stages of the ground motion or exclude reflected-wave effects, the contour, together with the lateral-domain sensitivity results, indicates that the final deformation pattern remains confined to the central domain and that crest-settlement predictions are largely insensitive to the tested domain widths.

6.3.5.2. Assumptions regarding pore-pressure treatment. In the adopted QUAKE/W Nonlinear formulation, simulating cyclic excess pore-water-pressure generation requires assigning the corresponding pore-pressure and recoverable-modulus functions [56]. These functions were not assigned to the embankment or foundation materials in the present analyses; consequently the initial hydrostatic pore-water-pressure distribution was retained throughout the dynamic analysis, and neither transient seepage nor cyclic excess pore-water-pressure generation was modeled. The simulations therefore represent cyclic deformation through nonlinear stress–strain behavior, strain-dependent stiffness reduction, and hysteretic energy dissipation rather than pore-pressure-induced effective-stress reduction. Accordingly, the adopted formulation does not account for earthquake-induced pore-pressure buildup, liquefaction-related strength loss, or post-liquefaction deformation, and it should not be interpreted as a fully coupled hydromechanical or liquefaction analysis. Such simplified uncoupled formulations have also been applied in seismic deformation analyses of embankment dams [75].

In the absence of site-specific cyclic pore-pressure measurements or laboratory calibration data, this simplification was adopted for the compacted embankment and stiff foundation materials represented in the present case study [5,62], consistent with deformation-based seismic assessment approaches [75,76]. It may however, underestimate deformation demand and damage-exceedance probabilities for loose, saturated, contractive, or liquefiable materials, in which excess pore-pressure buildup can reduce effective stress, stiffness, and shear strength, leading to larger permanent deformation and potentially shifting fragility curves toward lower intensity-measure levels [77–80]. Accordingly, the resulting probabilistic seismic demand models and fragility estimates are interpreted as conditional on the adopted deformation-based numerical formulation, rather than as predictions of liquefaction-induced response.

6.3.5.3. Numerical stability and demand extraction. For the representative strong-motion case, peak absolute normal strains remained below 0.25%, and no element distortion or mesh instability was observed, indicating satisfactory numerical stability in the examined analysis. For each ground-motion record, relative crest settlement was extracted as the EDP for development of the PSDMs. The resulting demand models were subsequently combined with the Bayesian seismic capacity model to derive the fragility relationships [81].

6.4. Benchmarking of the numerical model

The numerical model was based on the geometry and material properties of a real-world embankment dam reported by Guo et al. [55], originally studied by Mouyeaux et al. [57]. Because the reference dam lacks post-earthquake field measurements, site-specific validation was not possible; instead the model response was benchmarked against case histories and established empirical and experimental observations.

For deformation-based benchmarking, FEM-predicted crest settlements were compared with 21 case histories from the meta-database of 69 embankment dams compiled by Swaisgood [8], restricted to earth fill and hydraulic-fill dams consistent with the reference dam, with PGA $\leq$ 0.52 g and settlement $\leq$ 0.26 m. These case-history dams are not assumed to share the geometry, material properties, or site conditions of the reference dam but provide an empirical settlement range for broadly comparable responses. Park et al. [82] adopted a similar approach by comparing numerical crest settlements with Swaisgood case-history data over a range of PGA values while acknowledging differences in dam dimensions, material properties, and foundation profiles. The complete case-history dataset, including dam characteristics and earthquake information, is provided in Supplementary File 1 (Table S2). The numerical results reproduce the general trend of increasing crest settlement with PGA (Fig. 14a). The comparison yields an RMSE of 0.088 m (0.55% of dam height) and a mean bias of +0.052 m (0.33% of dam height). These measures indicate agreement with the documented settlement range and general PGA dependence. The dispersion among numerical predictions reflects record-to-record variability in the input motions, while scatter in the case-history data arises from differences in dam geometry, material properties, foundation conditions, seismic input characteristics, and measurement uncertainty, consistent with the dispersion reported by Park et al. [82]. Because the input motions were not matched to events recorded at individual case-history dams, this

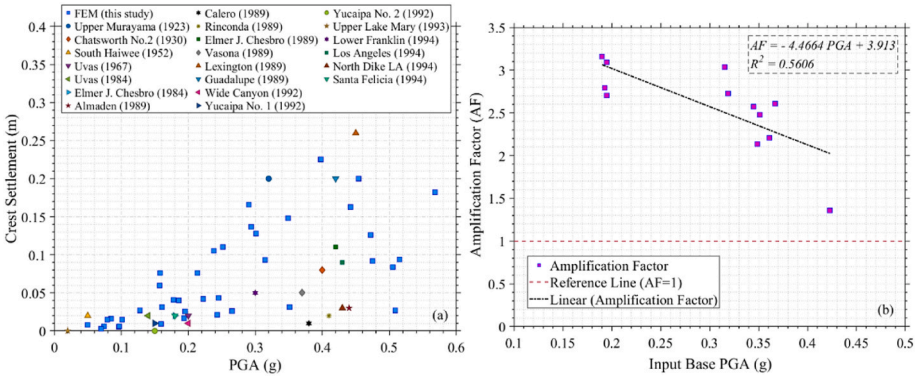


Fig. 14. Benchmarking of the numerical model: (a) comparison of FEM-predicted crest settlements with case-history data for embankment dams over a range of input base PGA; (b) relationship between crest amplification factor and PGA, including linear fit and reference line (AF = 1).

comparison addresses the overall settlement-versus-PGA range and trend rather than event-specific agreement.

Acceleration-response benchmarking was also performed for a subset of the input motions. Within this subset, the predicted crest amplification factors (AF), defined as $AF = PGA_{crest}/PGA_{input}$ range from approximately 1.5 to 3.2 and decrease with increasing PGA, consistent with increasing cyclic nonlinearity, secant-stiffness reduction, and hysteretic energy dissipation at higher strain levels (Fig. 14b). The fitted relationship ($AF = -4.47 \cdot PGA + 3.91$; $R^2 = 0.56$) captures this trend and applies only to this subset. The predicted amplification trend is consistent with observations from instrumented embankment dams [83], analytical shear-beam models [84], and centrifuge and strong-motion studies [82,85]. The empirical benchmarking is complemented by the lateral-domain sensitivity assessment presented in Section 6.3.5.1, which showed that crest settlement varied by no more than approximately 1.4% across the tested lateral extensions and that the final shear-strain concentrations remained confined to the central domain. Collectively, the settlement trends, indicative error measures, amplification behavior, and domain-sensitivity results support the numerical robustness and physical plausibility of the computed response within the considered PGA range but do not constitute site-specific validation. The model was therefore adopted for subsequent development of probabilistic seismic demand models.

7. Results of the case study application

7.1. Seismic demand models

PSDMs were developed to relate RS to selected IMs using log–log linear regression. The IMs considered include PGA, retained as a conventional acceleration-based baseline IM because it is widely used in seismic hazard assessment, seismic design practice, and existing dam fragility studies. Its inclusion provides a reference for comparison with previous deformation-based demand and fragility studies. PGV and VRMS were selected as velocity-related candidate IMs because the seismic response of embankment dams involves cyclic shear deformation, stiffness degradation, and accumulation of permanent settlement, which are influenced not only by peak acceleration but also by velocity characteristics and duration of ground motion. PGV represents peak velocity demand, whereas VRMS incorporates the full velocity time history and represents the overall velocity-amplitude content over the processed record duration. This physical interpretation is consistent with classical studies showing that earth dams and embankments behave as deformable dynamic systems whose seismic response depends on stiffness, geometry, material properties, foundation conditions, and excitation characteristics rather than on peak acceleration alone [86, 87]. Their inclusion is also supported by prior dam-focused IM-selection studies, which have identified velocity-based IMs as efficient predictors of deformation-sensitive embankment-dam response [10–14]. Accordingly, PGA, PGV, and VRMS were adopted as representative candidate IMs to evaluate how IM selection influences demand modeling and the resulting fragility estimates within the proposed Bayesian framework, rather than assuming that any single IM is universally optimal. Table 10 summarises the estimated regression parameters, including the intercept *a*, the scaling exponent *b*, the logarithmic standard deviation of demand σ_{lnD}, and the coefficient of determination R^2 [14]. Fig. 15 shows the corresponding regression relationships. These PSDMs provide a consistent probabilistic basis for developing fragility curves under both conventional acceleration-based and velocity-related IM representations.

Table 10
Parameters of probabilistic seismic demand models (PSDMs), including regression coefficients and statistical measures of demand dispersion and correlation.

IM	a	b	σ_{lnD}	R^2
PGA	0.0258	1.506	0.755	0.645
PGV	0.0186	1.276	0.678	0.714
VRMS	0.1250	1.195	0.813	0.588

7.2. Bayesian capacity model based fragility curves

Fragility curves based on the Bayesian seismic capacity models were developed for each IM by analytically combining the Bayesian capacity relationships with the corresponding PSDMs.

Following the uncertainty propagation procedure described in Section 5.1.2, posterior distributions of fragility were obtained by propagating paired posterior samples of the logarithmic median capacity (μ_{lnC}) and logarithmic dispersion (σ_{lnC}). Fig. 16 presents the resulting posterior median fragility curves together with the associated 95% credible intervals for PGA, PGV, and VRMS-based formulations across the Minor, Moderate, and Severe DSs. At low IM levels, the likelihood of exceeding the Minor DS increases quickly for all IMs, suggesting that relatively low levels of ground motion shaking are sufficient to cause minor deformation-related damage. The Moderate and Severe DSs on the other hand require increasingly higher IM levels to achieve comparable exceedance probabilities reflecting the rising deformation demands associated with more severe damage outcomes.

Across all IMs, the fragility curves exhibit smooth, distributed transitions between DSs rather than abrupt threshold-type behavior. The continuous shape of the fragility curves reflects the adopted probabilistic representation of seismic capacity and the resulting gradual increase in the probability of damage exceedance with increasing ground-motion intensity. The associated 95% credible intervals reflect the propagation of posterior uncertainty in the inferred capacity parameters through the analytical fragility formulation and generally widen for higher DSs, indicating greater uncertainty in predicting more severe DSs. Differences among the fragility curves derived using PGA, PGV, and

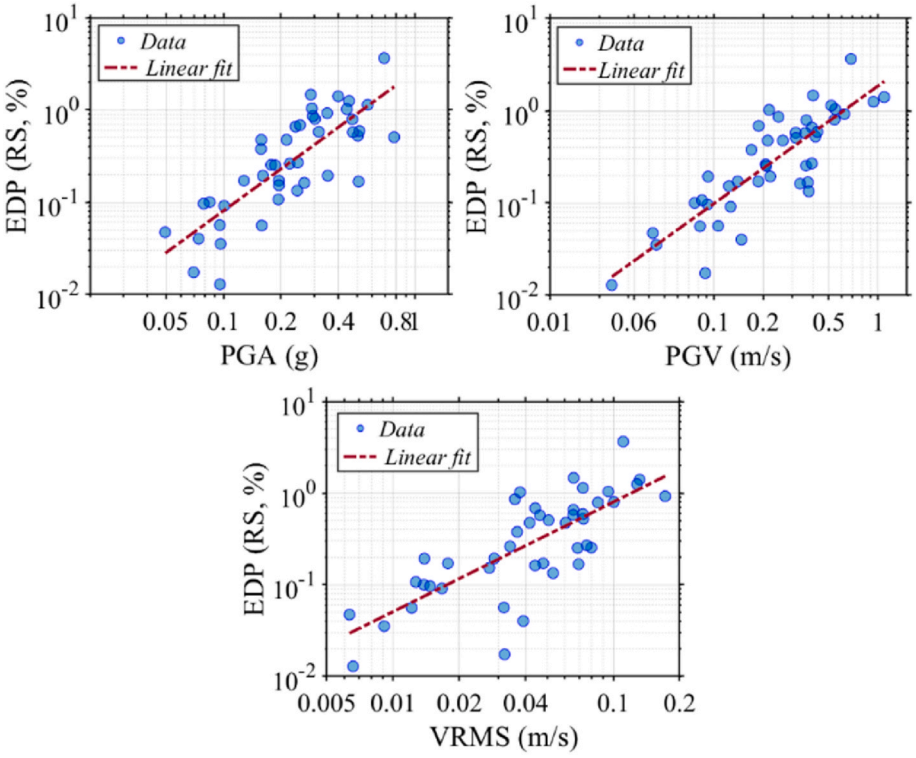


Fig. 15. Log-log regression models relating engineering demand parameter (EDP) to intensity measures (IMs). Points denote observed data, and dashed lines represent median demand predictions from the fitted power-law models. Axes are shown on logarithmic scales.

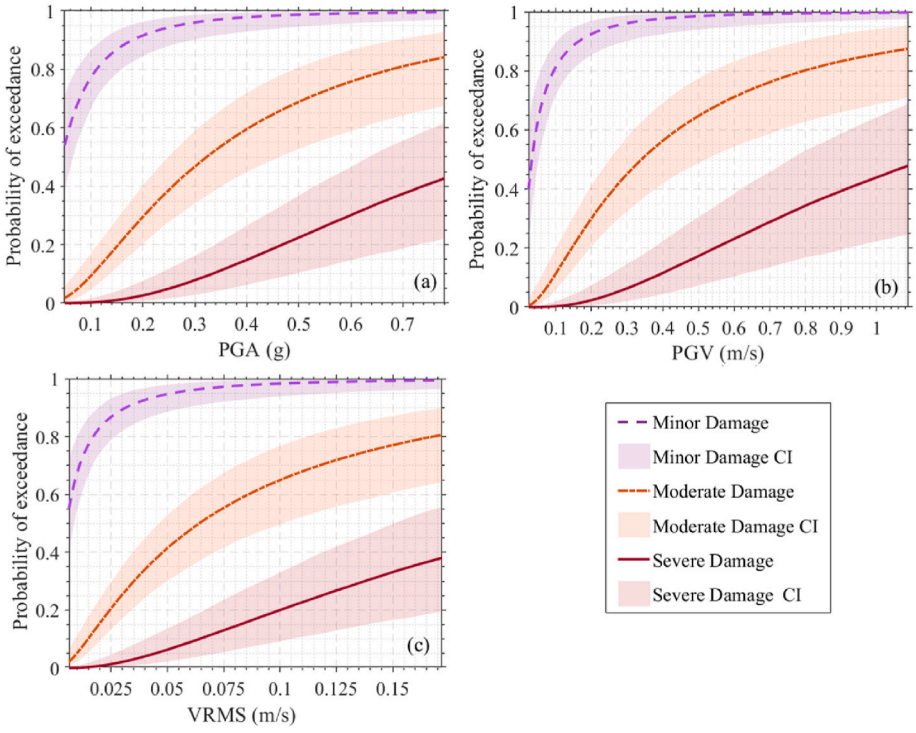


Fig. 16. Bayesian fragility curves for (a) PGA, (b) PGV, and (c) VRMS. Lines show posterior median fragility curves, and shaded regions denote the corresponding 95% credible intervals obtained by propagating posterior capacity-parameter uncertainty.

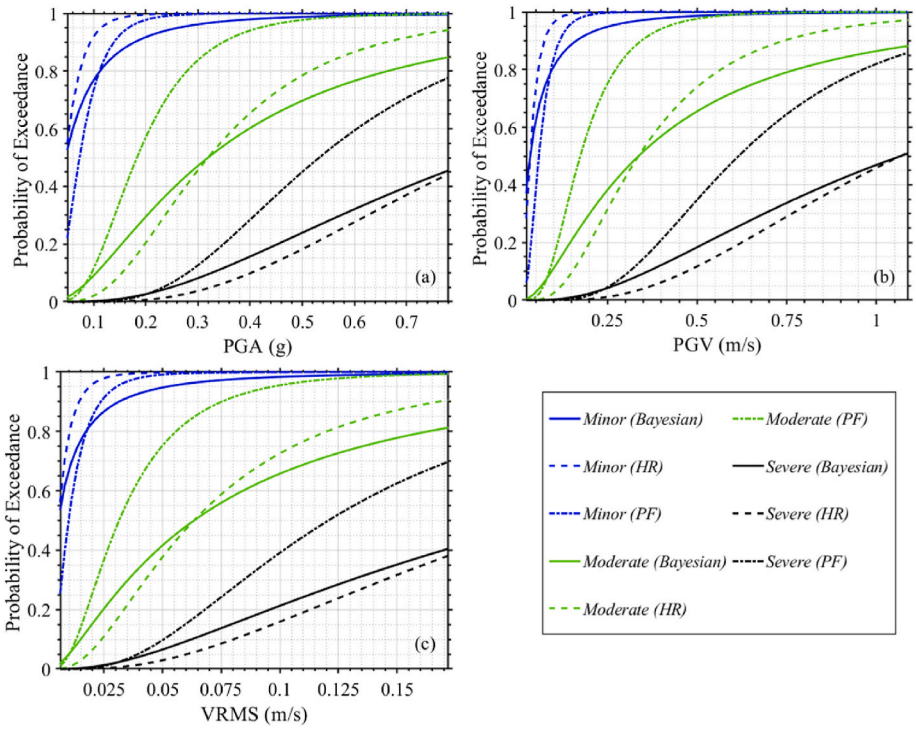


Fig. 17. Comparison of fragility curves obtained using identical probabilistic seismic demand models combined with three alternative capacity models: Bayesian (present study), He and Rathje (HR), and Pells and Fell (PF). Results are shown for (a) PGA, (b) PGV, and (c) VRMS.

VRMS are primarily governed by the relative efficiency and scaling characteristics of the underlying PSDMs. To assess sensitivity to demand-model selection, the posterior-median Bayesian capacity parameters were also combined with a PGV-based PSDM reconstructed from the published results of Khalid et al. [10]. This median-based comparison is presented for Minor and Moderate damage over the PGV range shared by both models in Section S3 of Supplementary File 2; segments below this shared range's lower limit are shown only for context. The present-study PSDMs remain the primary demand models for the case study application.

7.3. Comparison of fragility formulations across the capacity models

Fig. 17 compares fragility formulations derived using the Bayesian capacity model, the probabilistic capacity model proposed by He & Rathje [11] (HR), and the deterministic capacity model based on Pells & Fell [9] (PF) deformation thresholds, for PGA, PGV, and VRMS across all DSs. For all three capacity models the same PSDMs are employed, and the differences among the resulting fragility curves arise solely from the adopted capacity relationships. The Bayesian fragility curves are derived directly from the Bayesian capacity relationships developed in Fig. 5, whereas the HR and PF curves are obtained using the corresponding published capacity models. For all IMs, fragility curves exhibit the expected monotonic increase in DS exceedance probability with increasing IM, and the relative ordering of the three formulations remains consistent across DSs.

At low IM levels, the Bayesian, HR, and PF fragilities are closely aligned, indicating similar predictions for the onset of minor damage. As IM increases, systematic differences emerge. PF-based fragilities increase most rapidly, reaching high exceedance probabilities at comparatively lower IM levels. This behavior reflects the threshold-based nature of the PF capacity model which relies on fixed deformation limits and neglects capacity dispersion, leading to earlier transitions to higher DSs. HR based fragilities generally lie between the Bayesian and PF curves. Both the HR formulation and the central Bayesian formulation include capacity dispersion but they employ different median-capacity and dispersion parameters. Consequently, differences in their transition locations and slopes arise from differences between the fitted capacity relationships rather than from posterior parameter-uncertainty propagation, particularly for the Moderate and Severe DSs. In contrast, Bayesian fragilities increase more gradually with IM and exhibit smoother transitions across all DSs. This behavior reflects the median-capacity and capacity-dispersion parameters inferred from the individual case-history observations, which produce broader damage transitions over the analyzed IM range and yield lower exceedance probabilities at moderate to high IM levels.

The consistency of these trends across PGA, PGV, and VRMS indicates that the observed differences are primarily driven by capacity modeling assumptions rather than IM choice. While median fragility levels may be comparable at lower IM levels, capacity model selection substantially influences predicted damage exceedance at higher IM levels, with deterministic and threshold-based approaches generally producing more conservative fragility estimates than the Bayesian formulation.

7.4. Sensitivity of fragility estimates to capacity uncertainty

To assess the combined influence of capacity uncertainty and IM selection on seismic fragility estimates, analyses were performed for PGA and the velocity-based IMs (PGV and VRMS), considering four dispersion levels: deterministic ($\sigma_{\ln C} = 0$), reduced ($0.5\sigma_{\ln C}$), baseline ($1.0\sigma_{\ln C}$), and increased ($2.0\sigma_{\ln C}$). Fig. 18 shows the resulting sensitivity of the Bayesian fragility curves to capacity dispersion for PGA, PGV, and VRMS. Fragility curves for Minor, Moderate, and Severe DSs under each

IM indicate that increasing σ_{lnC} systematically flattens the curves, reflecting the smoothing effect of capacity dispersion on the deformation-capacity relationship. In this comparison the absolute difference is defined as the absolute difference in exceedance probability between a nonzero capacity dispersion fragility curve and the deterministic-capacity fragility curve at the same IM value:

$$\Delta P(IM) = \left| P\left(DS \geq k \middle| IM; m\sigma_{ln\ C,k}\right) - P\left(DS \geq k \middle| IM;\ \sigma_{ln\ C,k} = 0\right) \right| \ ;\ with\ m = 0.5, 1.0, 2.0 \tag{27}$$

where $\sigma_{lnC} = 0$ denotes the deterministic-capacity case, and m scales the baseline posterior median capacity dispersion (m = 0.5, 1.0, and 2.0 correspond to the reduced, baseline, and increased dispersion curves in Fig. 18). Thus, ΔP is expressed in probability points. For example, ΔP = 0.30 corresponds to a 30 percentage-point difference in exceedance probability, not a 30% change in IM or capacity.

For Minor damage, the maximum absolute probability differences relative to the deterministic case reach approximately 0.29 for PGA, 0.30 for PGV, and 0.28 for VRMS for the increased-dispersion case (m = 2.0, $\sigma_{ln\ C,k} = 2\sigma_{\ln C,k}^{baseline}$). For Moderate damage, the corresponding maximum absolute probability differences are approximately 0.25 for PGA, 0.26 for PGV, and 0.23 for VRMS. For Severe damage, the maximum differences are approximately 0.21 for PGA, 0.23 for PGV, and 0.20 for VRMS. These values indicate that Minor damage shows the largest maximum deviations from the deterministic-capacity case, followed by Moderate and Severe damage. This ordering follows directly from the baseline posterior median capacity dispersion, which is largest for Minor ($\sigma_{lnC} \approx 1.45$) and smallest for Severe ($\sigma_{lnC} \approx 0.87$): a larger capacity dispersion produces a larger departure from the deterministic-capacity curve. The influence of capacity dispersion is most evident near the transition region of each fragility curve, where the fragility curves are steepest. These discrepancies demonstrate that neglecting capacity dispersion can change estimated exceedance probabilities by approximately 0.20–0.30 probability points within the analyzed IM ranges, highlighting the potential for bias if capacity dispersion is neglected. For the present case study, the maximum probability-point differences are of comparable magnitude across PGA, PGV, and VRMS, although VRMS gives slightly smaller deviations than PGA for all three DSs. PGV produces deviations comparable to those of PGA. These results indicate that

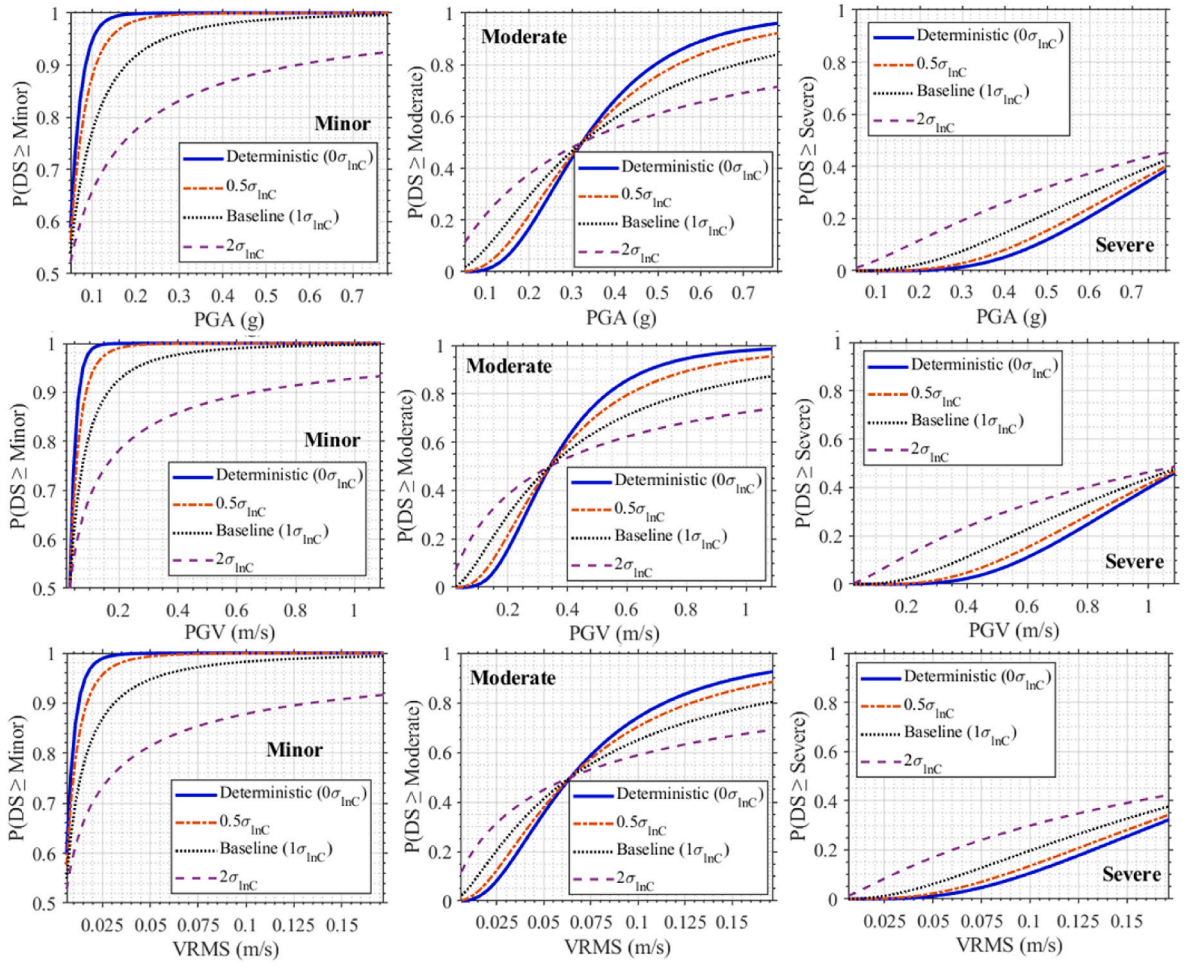


Fig. 18. Sensitivity of Bayesian capacity model-based seismic fragility curves to uncertainty in logarithmic capacity dispersion (σ_{lnC}) across intensity measures and damage states. Rows correspond to intensity measures (top to bottom: PGA, PGV, and VRMS), and columns correspond to damage states (left to right: Minor, Moderate, and Severe). Fragility curves are shown for deterministic capacity ($\sigma_{lnC} = 0$), reduced capacity dispersion ($0.5\sigma_{lnC}$), baseline Bayesian capacity dispersion ($1\sigma_{lnC}$), and increased capacity dispersion ($2\sigma_{lnC}$).

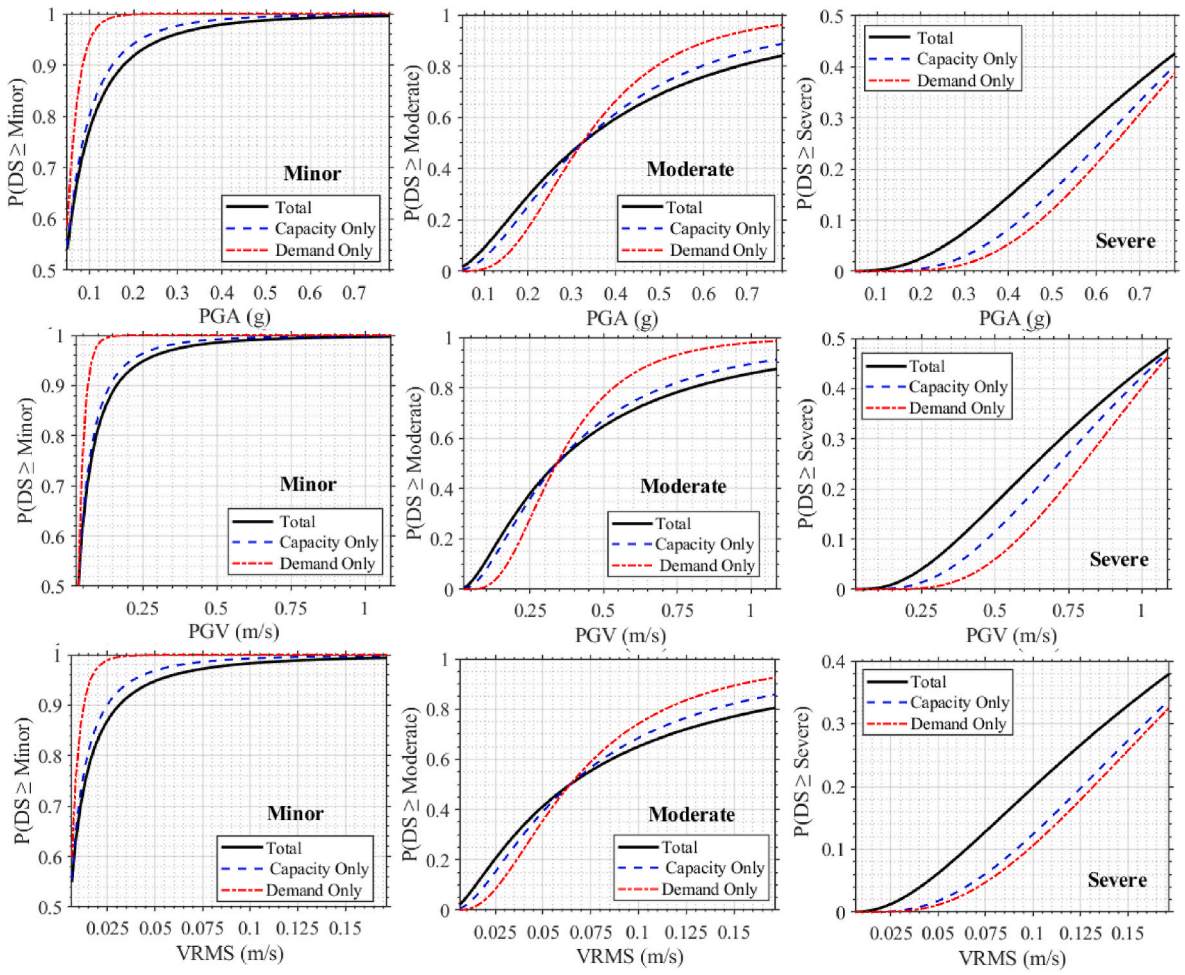


Fig. 19. Decomposition of total fragility uncertainty into capacity and demand-driven components for different ground motion intensity measures. The probability of exceeding minor, moderate, and severe damage states is shown for each intensity measure, with the total fragility (solid black line), capacity-driven contribution (dashed blue line), and demand-driven contribution (dash-dotted red line). (For interpretation of the references to colour in this figure legend, the reader is referred to the Web version of this article.)

Table 11
Damage exceedance probabilities P(DS ≥ k) at the 10th, 50th, and 90th percentile IM levels of the selected input ground-motion suite.

IM	Damage state	IM_{10}	P(DS ≥ k) [95% CI]	IM_{50}	P(DS ≥ k) [95% CI]	IM_{90}	P(DS ≥ k) [95% CI]
PGA (g)	Minor	0.084	0.723 [0.616–0.833]	0.241	0.941 [0.873–0.976]	0.510	0.988 [0.945–0.998]
	Moderate	0.084	0.064 [0.028–0.132]	0.241	0.369 [0.267–0.479]	0.510	0.696 [0.537–0.811]
	Severe	0.084	0.001 [0.000–0.011]	0.241	0.042 [0.014–0.108]	0.510	0.228 [0.109–0.377]
PGV (m/s)	Minor	0.082	0.768 [0.667–0.862]	0.234	0.942 [0.872–0.978]	0.555	0.988 [0.944–0.998]
	Moderate	0.082	0.079 [0.035–0.155]	0.234	0.354 [0.250–0.465]	0.555	0.684 [0.523–0.806]
	Severe	0.082	0.001 [0.000–0.014]	0.234	0.033 [0.010–0.096]	0.555	0.201 [0.092–0.348]
VRMS (m/s)	Minor	0.013	0.736 [0.633–0.840]	0.045	0.940 [0.873–0.974]	0.102	0.983 [0.938–0.996]
	Moderate	0.013	0.077 [0.038–0.146]	0.045	0.379 [0.277–0.486]	0.102	0.654 [0.506–0.768]
	Severe	0.013	0.002 [0.000–0.014]	0.045	0.050 [0.018–0.117]	0.102	0.200 [0.097–0.335]

Note: IM_{10}, IM_{50}, and IM_{90} denote the 10th, 50th, and 90th percentile values of the selected input ground-motion suite for each intensity measure (PGA, PGV, and VRMS). These percentile-based IM values are descriptive statistics of the selected ground-motion suite and are not derived from a probabilistic seismic hazard analysis (PSHA).

the sensitivity of fragility estimates to capacity dispersion depends on the selected IM, DS, and characteristics of the fitted demand model.

7.5. Contribution of capacity and demand uncertainty

The total fragility dispersion was decomposed into capacity and demand related components to quantify their relative contributions for each IM and DS, and the results are shown in Fig. 19. For Minor damage, capacity dispersion dominates across all IMs. The ratio of capacity variance to total variance ranges from approximately 76% for VRMS to 82% for PGV and 79% for PGA, indicating that capacity-related variability largely controls the total fragility dispersion at low damage levels. Correspondingly, the demand-related contribution remains modest (≈18%–24%), reflecting the limited influence of record-to-record variability. The capacity-only, demand-only, and total fragility curves exhibit different transition slopes and deviate most noticeably within the transition region, with the total response governed predominantly by the capacity-related component for Minor damage.

For Moderate damage, the influence of demand-related variability increases. Capacity variance ratios decrease to approximately 64%–72% across IMs, while demand variance ratios rise to 28%–36%. Consequently, both capacity and demand contribute significantly to the total fragility dispersion, with the gap between the capacity-only and demand-only curves becoming more pronounced. This indicates a transition from predominantly capacity-driven dispersion at lower damage levels to a mixed influence at Moderate damage levels. For Severe damage, the demand-related contribution increases substantially and approaches the capacity-related contribution. Capacity variance ratios drop to 54%–63%, while demand variance ratios reach 37%–46%. Thus, capacity remains the larger component, although the relative influence of demand variability is considerably greater than for the Minor and Moderate DSs. The capacity-only and demand-only curves exhibit different transition slopes and deviate from the total fragility curve primarily within the transition region. The largest demand-related contribution occurs for VRMS (≈46%), followed by PGA (≈42%) and PGV (≈37%), reflecting differences in the residual dispersions of the corresponding PSDMs. Among the selected IMs, VRMS therefore gives the largest demand-related contribution for Severe damage, followed by PGA and PGV.

7.6. Effect of capacity model choice on risk-based metrics

Table 11 reports the 10th, 50th, and 90th percentile IM values of the selected ground-motion suite and the corresponding posterior-median DS exceedance probabilities with 95% credible intervals for PGA, PGV, and VRMS. These descriptive levels represent low, central, and high intensities within the analyzed range and are not derived from a site-specific hazard analysis. Exceedance probabilities increase monotonically with IM; at the 10th percentile, Minor-damage exceedance is approximately 0.72, 0.77, and 0.74 for PGA, PGV, and VRMS , respectively, while Moderate and Severe exceedance increase more strongly with seismic demand.

At corresponding percentile-based IM levels, the DS exceedance probabilities are generally comparable across PGA, PGV, and VRMS. At the central (50th percentile) IM level, Moderate-damage exceedance is approximately 0.369 for PGA, 0.354 for PGV, and 0.379 for VRMS. At the upper (90th percentile) IM level, Severe-damage exceedance reaches approximately 0.228 for PGA, 0.201 for PGV, and 0.200 for VRMS. Although the posterior median estimates differ slightly, the corresponding 95% credible intervals overlap substantially, and no single IM consistently produces higher exceedance probabilities across the representative percentile levels. The observed variations arise from the combined influence of the PSDM intercept, scaling coefficient, and residual dispersion, which govern the location and transition slope of the fragility curves for each IM.

Fig. 20 presents the EDI as a function of IM for fragilities derived from the Bayesian, HR, and PF capacity models. At lower IM values, the PF curve initially lies below the Bayesian and HR curves, subsequently crosses them, and increases more rapidly with IM. The Bayesian and HR curves remain closely aligned throughout the analyzed ranges, with the HR curve generally lying within the Bayesian 95% credible interval. At representative mid-range intensities of PGA≈0.30g, PGV≈0.40 m/s, and VRMS≈0.07 m/s, the Bayesian EDI values are approximately 1.51, 1.71, and 1.63, respectively, whereas the corresponding PF values are approximately 1.97, 2.21, and 2.11. At these intensities, the PF and HR formulations produce EDI values approximately 29%–30% and 1%–3% higher, respectively, than the Bayesian formulation. The maximum vertical separation between the PF and Bayesian curves is approximately 0.5 EDI units across the considered IM ranges. The separation among the capacity-model formulations varies with the scaling and residual-dispersion characteristics of the corresponding PSDMs. Unlike the fixed-parameter HR and PF formulations, the Bayesian model

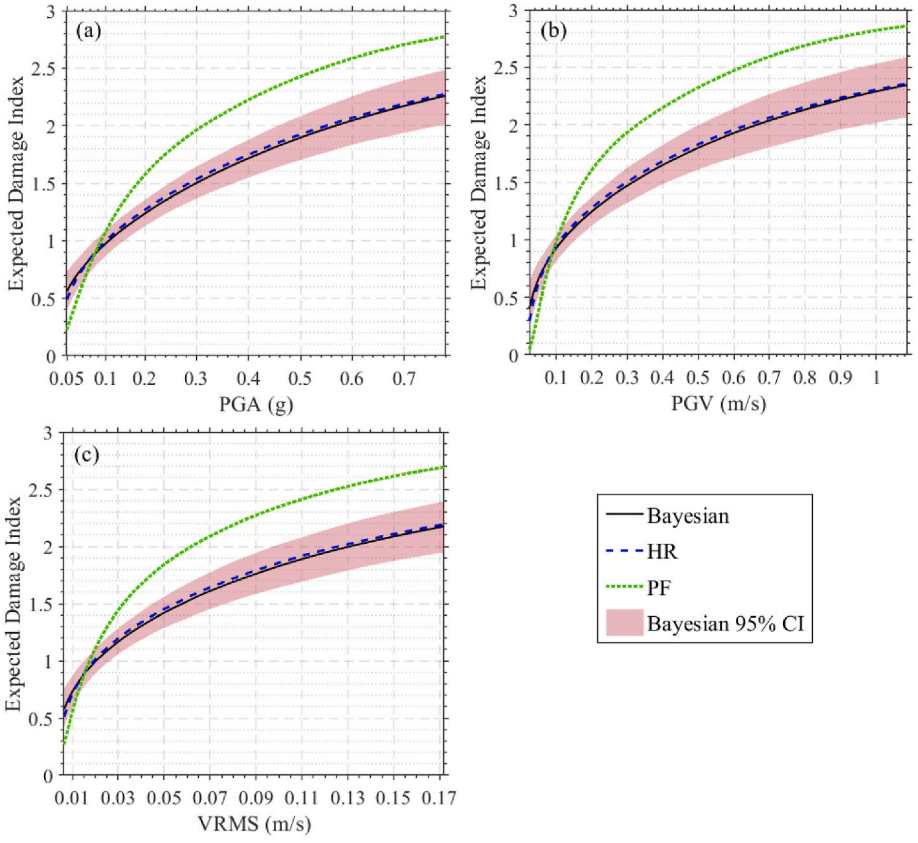


Fig. 20. Expected Damage Index (EDI) as a function of intensity measure for PGA, PGV, and VRMS , showing the Bayesian posterior median and 95% credible interval together with the fixed-parameter He and Rathje (HR) and Pells and Fell (PF) formulations.

propagates posterior uncertainty in the capacity parameter into the EDI calculation, yielding posterior-median EDI curves and 95% credible intervals. These differences could influence comparative damage estimates and EDI-based prioritization when considered alongside site-specific hazard, exposure, and consequence information. Overall, the influence of capacity-model choice is limited at low IMs but increases at moderate to high IMs. Among the considered models, only the Bayesian formulation propagates capacity-parameter uncertainty into the EDI, yielding posterior-median curves with 95% credible intervals rather than single-point estimates.

8. Implications for risk-informed decision making for existing embankment dams

The Bayesian capacity framework has two practical implications for the risk-informed management of existing embankment dams, which are addressed in the following subsections.

8.1. Decision confidence beyond median fragility

The generalized Bayesian seismic capacity model developed in this study can be combined with a dam-specific PSDM to develop IM-based fragility curves for an existing embankment dam. The resulting fragility relationships therefore reflect both the generalized deformation-based capacity model and the seismic demand characteristics of the individual dam. In practice, engineering decisions depend not only on the estimated probability of damage exceedance but also on the confidence associated with that estimate. For a given IM level, let P_k(IM) denote the posterior distribution of the probability of exceeding k^{th} DS. In the Bayesian framework, posterior uncertainty relevant to decision making can be quantified using ΔP_k(IM), defined as:

$$\Delta P_k(IM) = P_k^{95\%}(IM) - P_k^{50\%}(IM) \tag{28}$$

where $P_k^{50\%}$(IM) and $P_k^{95\%}$(IM) represent the posterior median exceedance probability and the upper bound of its two-sided 95% credible interval, respectively, at the same IM value. Thus, ΔP_k(IM) represents the upper posterior uncertainty margin in exceedance probability rather than the full width of the 95% credible interval. As shown in Section 7.2 (Fig. 16), the posterior median fragility curves may resemble the deterministic-capacity curves while still exhibiting non-negligible credible intervals, particularly for the Moderate and Severe DSs. Consequently, ΔP_k(IM) provides a quantitative measure of confidence in the estimated exceedance probability, with larger values indicating greater uncertainty in predicted performance. Within the proposed Bayesian framework, ΔP_k(IM) is obtained directly from the posterior distribution of the fragility curves through propagation of capacity-parameter uncertainty, whereas deterministic capacity models collapse this uncertainty into a single estimate and provide no explicit measure of confidence. Consequently, two dams with comparable posterior median exceedance probabilities but different ΔP_k(IM) are not equivalent for decision-making: the dam with the larger ΔP_k(IM) carries lower confidence in its predicted performance and therefore warrants greater scrutiny before rehabilitation or retrofit decisions are finalized. A worked example demonstrating the application of ΔP_k(IM) is provided in Appendix C.

8.2. Capacity uncertainty and risk-based prioritization

Risk-informed management of dam portfolios commonly relies on comparative ranking rather than absolute risk values. In practice, such prioritization is often based on scalar risk metrics, such as the EDI, which aggregates DS occurrence probabilities using the ordinal severity weights defined in Section 5.2. As described there, EDI is bounded between 0 and 3 and is interpreted here as a relative measure of expected damage severity for comparing the effects of alternative capacity models on risk prioritization. For two existing embankment dams, the relative difference in expected damage severity may be expressed as:

$$\Delta EDI_{ij}(IM) = EDI_i(IM) - EDI_j(IM) \tag{29}$$

where EDI_i *(IM)* and EDI_j *(IM)* denote the Expected Damage Indices of dams i and j, respectively, evaluated at the same IM level. A positive ΔEDI_{ij} value indicates that dam i exhibits greater expected damage severity at the specified IM level and therefore a higher priority for detailed assessment or retrofit, whereas a negative value indicates a higher priority for dam j. This comparison can support prioritization for detailed assessment, monitoring, rehabilitation, or retrofit when considered together with site-specific hazard, exposure, and consequence information. Although explicit portfolio-ranking probabilities are not computed in this study, the EDI comparisons presented in Section 7.6 demonstrate that alternative capacity models produce materially different EDI-intensity trajectories. These results indicate that the choice of capacity model can alter comparative risk assessments, particularly for dams with similar median performance, thereby influencing the prioritization of rehabilitation, monitoring, or retrofit measures. A worked example illustrating the complementary application of ΔP_k(IM) and ΔEDI_{ij}(IM) is provided in Appendix C.

9. Conclusions

The increasing focus on performance-based assessment of critical infrastructure including embankment dams, underscores the need for seismic evaluation frameworks that explicitly account for uncertainty in both seismic demand and capacity. This study presents a Bayesian framework for uncertainty-informed, deformation-based seismic capacity modeling for embankment dams and illustrates its direct integration into fragility and risk assessment within a PBEE framework. The framework is developed using 94 heterogeneous earthquake case histories of which 91 DS1–DS4 records are retained for capacity-model calibration, with seismic performance quantified using relative crest settlement. Analysis of these data reveals systematic yet highly variable relationships between deformation demand and DS exceedance, highlighting the inadequacy of deterministic deformation thresholds and motivating probabilistic capacity formulations that explicitly represent uncertainty in damage initiation and progression. The proposed Bayesian seismic capacity models are integrated with PSDMs in a fragility and risk analysis of a 16 m high embankment dam case study. Fragility curves are developed using three representative intensity measures (PGA, PGV, and VRMS), with aleatory variability in seismic demand captured through residual dispersion. Posterior uncertainty in the Bayesian capacity parameters is propagated through the analytical fragility formulation to obtain posterior distributions of fragility, from which posterior median fragility curves and 95% credible intervals are derived supporting a fully probabilistic evaluation of damage-state exceedance. The major findings of this study are summarised as follows:

- DS exceedance increases gradually with RS, indicating that damage initiation and progression are not governed by sharp thresholds. Bayesian capacity models provide continuous capacity relationships with posterior medians and 95% credible intervals that explicitly quantify posterior uncertainty in the inferred capacity parameters.
- Damage state-dependent capacity models inferred via Bayesian probit regression and MCMC sampling yield stable, unimodal posterior distributions for both the log-median and dispersion parameters ($\mu_{\ln C,k}$, $\sigma_{\ln C,k}$). Convergence diagnostics and posterior predictive checks confirm statistical adequacy and consistency with observed damage frequencies. Posterior estimates are robust to alternative prior specifications.
- Bayesian fragility models provide posterior median exceedance relationships together with 95% credible intervals obtained by propagating posterior uncertainty in the inferred capacity parameters

through the analytical fragility formulation. The sensitivity of fragility estimates to capacity uncertainty depends on the selected IM and DS. The selection of the capacity modeling framework therefore materially affects risk-based decision outcomes, particularly under moderate to high intensity conditions.

- Fragility curves systematically flatten with increasing capacity dispersion. Minor damage shows the largest maximum deviations from the deterministic-capacity case (≈0.28–0.30 across IMs), followed by Moderate (≈0.23–0.26) and Severe damage (≈0.20–0.23); this ordering follows the posterior capacity dispersion, which is largest for Minor and smallest for Severe. Across IMs, the maximum probability-point differences are of comparable magnitude, with VRMS giving the smallest deviations and PGA and PGV comparable.
- Capacity dispersion dominates Minor damage, while both capacity and demand contribute substantially to Moderate damage. For Severe DS, the demand-related contribution increases to approximately 37%–46% and approaches the capacity-related contribution, although capacity remains the larger component across all IMs. The demand-related contribution reaches approximately 42% for PGA and 46% for VRMS. Among the selected IMs, VRMS exhibits the largest demand-related contribution for Severe damage.
- Comparisons among the Bayesian, HR, and PF formulations reveal systematic differences in EDI. At the representative mid-range intensities considered, PF and HR based EDI values are approximately 29%–30% and 1%–3% higher, respectively than the Bayesian values, while the maximum PF–Bayesian separation is approximately 0.5 EDI units. The Bayesian formulation additionally provides posterior-median EDI curves and 95% credible intervals by propagating uncertainty in the capacity parameter. These differences may affect comparative damage estimates and EDI-based prioritization, although no explicit portfolio-ranking analysis was performed.

Overall, the results demonstrate that explicit probabilistic modeling of seismic capacity within a Bayesian framework enables posterior uncertainty in the inferred capacity parameters to be propagated into fragility estimates while preserving data-informed median fragility relationships. The resulting posterior median fragility curves and associated 95% credible intervals provide a robust basis for uncertainty-informed seismic risk assessment of embankment dams. Among the models considered, the Bayesian formulation provides the most statistically complete and uncertainty-consistent assessment, although its predictive performance requires independent validation, and the present results remain subject to the data and modeling scope detailed in Section 10.

10. Limitations and future work

This study has two limitations. First, the seismic capacity models are inferred from available earthquake case history data, which remain limited in quantity and heterogeneous in terms of dam characteristics, seismic environments, and damage reporting practices. The Bayesian inference framework explicitly quantifies capacity uncertainty through posterior parameter distributions; however, the inferred capacity relationships remain conditioned on the quality and representativeness of the available observations. As additional post-earthquake data with consistent damage classification and deformation measurements become available, the capacity distributions can be systematically updated within the same framework, progressively reducing capacity uncertainty. Second, the seismic demand models for relative crest settlement are derived from nonlinear dynamic finite-element analyses of a single embankment dam geometry with a height of 16 m. This modeling choice enables controlled evaluation of IMs and consistent uncertainty propagation but is not intended to be universally applicable. Applying the framework to dams with substantially different geometries, dam heights, construction materials, foundation conditions, or seismic environments would therefore require redevelopment or recalibration of the demand relationships through geometry and site-specific numerical analyses; for example, a taller embankment dam such as a 50 m dam would require a separate finite-element model and PSDM because dam height affects the stress state, dynamic characteristics, and deformation demand.

Future work may extend the proposed framework to multiple dam geometries, different dam-height classes, three-dimensional numerical simulations, and fully coupled effective-stress hydro-mechanical analyses incorporating cyclic excess pore-water-pressure generation, thereby representing the evolution of pore-water pressure and its effects on effective stress, stiffness, shear strength, and permanent deformation demand, and enhancing applicability to site-specific risk assessments. The proposed Bayesian capacity and fragility framework can incorporate demand results from these simulations when compatible EDP and DS data are available. Although PGA, PGV, and VRMS provide representative acceleration-based and velocity-related IMs for the present comparison, future studies may also examine additional scalar and vector IMs to support demand-model development. From a computational perspective application to larger datasets or hierarchical model formulations may benefit from advanced sampling algorithms, such as Hamiltonian Monte Carlo, to improve sampling efficiency and scalability.

CRediT authorship contribution statement

Surya Prakash: Writing – original draft, Visualization, Validation, Software, Methodology, Investigation, Formal analysis, Data curation, Conceptualization. **P. Anbazhagan:** Writing – review & editing, Supervision, Project administration, Funding acquisition.

Declaration of competing interest

The authors declare that they have no known competing financial interests or personal relationships that could have appeared to influence the work reported in this paper.

Acknowledgements

The authors would like to thank the Dam Safety (Rehabilitation) Directorate, Central Water Commission (CWC) for funding the “International Centre of Excellence in Dam Engineering” (ICED) under the Dam Rehabilitation and Improvement Project (DRIP); Ministry of Jal Shakti (MoJS), Government of India for the project entitled “Integrated Investigation for Risk Assessment of the Dam” under grant R-24011/57/2023-Pen Riv Section-MOWR.

Appendix D. Supplementary data

Supplementary data to this article can be found online at https://doi.org/10.1016/j.soildyn.2026.110740.

Appendix A. Derivation of IM-Based Fragility from the EDP-Space Capacity Model

The Bayesian capacity model is first defined in engineering demand parameter (EDP) space, where the EDP is the relative crest settlement, RS. For

damage state k, each posterior sample s of the capacity parameters ($\mu^{(s)}_{\ln C,k}$, $\sigma^{(s)}_{\ln C,k}$) gives the conditional probability of DS exceedance as:

$$P^{(s)}(DS \geq k|RS) = \Phi\left[\frac{\ln RS - \mu^{(s)}_{\ln C,k}}{\sigma^{(s)}_{\ln C,k}}\right] \tag{A1}$$

where $\mu^{(s)}_{\ln C,k}$ and $\sigma^{(s)}_{\ln C,k}$ are the posterior-sampled logarithmic median and dispersion of the relative crest settlement capacity, respectively, and $\Phi(\cdot)$ is the standard normal cumulative distribution function. The probabilistic seismic demand model (PSDM) relates the EDP to the selected IM as:

$$\ln(RS) = \ln a + b\cdot\ln(IM) + \varepsilon \tag{A2}$$

where a and b are PSDM regression coefficients and ε is the residual demand term. Assuming $\varepsilon \sim N(0,\sigma^2_{lnD})$, the demand distribution conditional on IM is:

$$\ln RS|IM \sim N(\ln a + b\cdot\ln(IM), \sigma^2_{lnD}) \tag{A3}$$

For posterior sample s, the logarithmic capacity corresponding to damage state k is:

$$\ln C^{(s)}_k \sim N\left(\mu^{(s)}_{\ln C,k}, \left(\sigma^{(s)}_{\ln C,k}\right)^2\right) \tag{A4}$$

Damage state k is exceeded when seismic demand exceeds capacity. Therefore,

$$P^{(s)}(DS \geq k|IM) = P\left(\ln RS - \ln C^{(s)}_k > 0\middle|IM\right) \tag{A5}$$

Assuming demand and capacity are statistically independent conditional on IM, the difference $\ln RS - \ln C^{(s)}_k$ is normally distributed as:

$$\ln RS - \ln C^{(s)}_k \sim N\left[\ln a + b\ln(IM) - \mu^{(s)}_{\ln C,k}, \sigma^2_{lnD} + \left(\sigma^{(s)}_{\ln C,k}\right)^2\right] \tag{A6}$$

Thus, the posterior-sampled fragility function in IM space is:

$$P^{(s)}(DS \geq k|IM) = \Phi\left[\frac{\ln a + b\cdot\ln(IM) - \mu^{(s)}_{\ln C,k}}{\sqrt{\left(\sigma^{(s)}_{\ln C,k}\right)^2 + \sigma^2_{\ln D}}}\right] \tag{A7}$$

Equation (A7) can be rearranged into the standard lognormal IM-based fragility form:

$$P^{(s)}(DS \geq k|IM) = \Phi\left[\frac{\ln(IM) - \mu^{(s)}_{IM,k}}{\beta^{(s)}_{IM,k}}\right] \tag{A8}$$

where:

$$\mu^{(s)}_{IM,k} = \frac{\mu^{(s)}_{\ln C,k} - \ln a}{b} \tag{A9}$$

and

$$\beta^{(s)}_{IM,k} = \frac{\sqrt{\left(\sigma^{(s)}_{\ln C,k}\right)^2 + \sigma^2_{lnD}}}{b} \tag{A10}$$

The ensemble of sampled curves $P^{(s)}(DS \geq k|IM)$, for $s = 1,\ldots,S$, defines the posterior distribution of the fragility curve at each IM value. The median fragility curve and the 95% credible interval are obtained from the 50th, 2.5th, and 97.5th percentiles of this ensemble. This derivation shows that the EDP-space Bayesian capacity model is mapped into IM space through the PSDM; the EDP and IM based formulations are therefore linked through the demand model but are not interchangeable.

Appendix B. Definition and Computation of Ground-Motion Intensity Measures

For each input motion, ground motion IMs (PGA, PGV, and VRMS) were computed using SeismoSignal Software [88] from the processed acceleration time history.

- PGA and PGV were defined as the maximum absolute acceleration and velocity of ground motion, respectively [5]:

$$PGA = \max|a(t)| \tag{B1}$$

$$PGV = \max|v(t)| \tag{B2}$$

where a(t) is the ground acceleration time history and v(t) is the corresponding velocity time history obtained by integrating the processed acceleration record.

- VRMS is the root mean square velocity over the record [5] and is defined as:

$$VRMS = \sqrt{\frac{1}{t_{total}} \int_0^{t_{total}} [v(t)]^2 dt} \tag{B3}$$

where t_{total} is the total duration of the processed input record. Thus, VRMS was computed over the full processed record duration using the SeismoSignal ground-motion-parameter definition, rather than over a manually selected strong-motion or threshold-based shaking window.

Appendix C. Illustrative Use of the Decision Metrics

The complementary roles of $\Delta P_k(IM)$ and ΔEDI_{ij} are illustrated using a hypothetical example involving two existing embankment dams. The generalized Bayesian capacity model developed in this study is assumed to be combined with dam-specific PSDMs to develop fragility curves and the corresponding EDIs for both dams. The numerical values presented below are illustrative and are intended solely to demonstrate the decision-making workflow described in Section 8. At a specified IM level, suppose both dams have the same posterior median probability of exceeding the Moderate DS, $P_k^{50\%}(IM) = 0.60$. Let the corresponding upper bounds of the two-sided 95% credible intervals be $P_k^{95\%}(IM) = 0.75$ for Dam A and 0.62 for Dam B. The resulting uncertainty measures are therefore $\Delta P_k(IM) = 0.15$ and 0.02, respectively. Although both dams have identical $P_k^{50\%}(IM)$, the substantially larger uncertainty associated with Dam A indicates lower confidence in the predicted seismic performance and suggests that additional site investigation, monitoring, or material characterization may be warranted before engineering decisions are made.

The same two dams can also be compared using the EDI as a scalar risk metric. At the same IM level, suppose that the Bayesian framework yields $EDI_A = 1.85$ and $EDI_B = 1.60$, giving $\Delta EDI_{AB} = 0.25$. This indicates that Dam A is expected to experience greater overall damage severity at the specified IM level and could therefore receive higher priority for detailed assessment or retrofit when considered together with site-specific hazard, exposure, and consequence information. Thus, the two metrics serve complementary purposes: $\Delta P_k(IM)$ is first used to assess confidence in the fragility prediction for an individual dam, while the EDI subsequently supports comparative prioritization among dams, together providing a structured basis for uncertainty-informed decision-making for existing embankment dams.

Data availability

The case-history data used for Bayesian capacity-model calibration are available from the DesignSafe-CI dataset of He and Rathje [35] (DOI: https://doi.org/10.17603/ds2-pwtv-p173). Supplementary File 1 in Appendix D provides the metadata and computed intensity measures for the input ground-motion records, together with the published case-history records used for numerical-model benchmarking. The input ground-motion records were obtained from the COSMOS Strong-Motion Virtual Data Center (https://www.strongmotioncenter.org), and their corresponding record identifiers are provided in Supplementary File 1 (Table S1). The native QUAKE/W files and simulation results generated in this study form part of the deliverables of the ongoing research project funding this work and remain in use; they therefore cannot be shared.

References

[1] Beck MW, Claassen AH, Hundt PJ. Environmental and livelihood impacts of dams: common lessons across development gradients that challenge sustainability. Int J River Basin Manag Mar. 2012;10(1):73–92. https://doi.org/10.1080/15715124.2012.656133.

[2] Busch AM. Dams and the age of abundance: hydraulic boosterism, regional growth, and the reemergence of water scarcity in central Texas. J Urban Hist Mar. 2023;49(2):309–34. https://doi.org/10.1177/00961442211008865.

[3] Singh R, Roy D, Das D. A correlation for permanent earthquake-induced deformation of earth embankments. Eng Geol Mar. 2007;90(3):174–85.

[4] Makdisi FI, Seed HB. Simplified procedure for estimating dam and embankment earthquake-induced deformations. J Geotech Eng Div Jul. 1978;104(7):849–67.

[5] Kramer SL, Stewart JP. Geotechnical earthquake engineering. CRC Press; 2024.

[6] Xiao-long L, Shi-chun CHI. Seismic reliability analysis of high earth-rockfill dams based on deformation control criteria. Chin J Geotech Eng Mar. 2019;41(3):519–25.

[7] Anbazhagan P, Prakash S. Novel seismic dam damage intensity scale and empirical models for predicting seismically induced damages in embankment dams. Soil Dynam Earthq Eng Apr. 2026;203:110079. https://doi.org/10.1016/j.soildyn.2025.110079.

[8] Swaisgood R. Embankment dam deformations caused by earthquakes. 2003.

[9] Pells S, Fell R. Damage and cracking of embankment dams by earthquakes and the implications for internal erosion and piping. University of New South Wales, School of Civil and Environmental Engineering; 2003.

[10] Irslan Khalid M, Park D, Fei J, Nguyen V-Q, Nguyen D-D, Chen X. Selection of efficient earthquake intensity measures for evaluating seismic fragility of concrete face rockfill dam. Comput Geotech Nov. 2023;163:105721. https://doi.org/10.1016/j.compgeo.2023.105721.

[11] He J, Rathje EM. Seismic capacity models for earth dams and their use in developing fragility curves. Earthq Spectra Aug. 2024;40(3):1986–2007.

[12] Regina G, Zimmaro P, Ziotopoulou K, Cairo R. Evaluation of the optimal ground motion intensity measure in the prediction of the seismic vulnerability of earth dams. Earthq Spectra Nov. 2023;39(4):2352–78. https://doi.org/10.1177/87552930231170894.

[13] Rathje EM, He J. A seismic fragility framework for Earth dams. Nov. 2022. p. 405–15. https://doi.org/10.1061/9780784484432.036.

[14] Prakash S, Anbazhagan P. Optimal ground motion intensity measures for the seismic vulnerability assessment of embankment dams. Georisk Assess Manag Risk Eng Syst Geohazards Jan. 2026:1–30. https://doi.org/10.1080/17499518.2026.2614741. vol. 0, no. 0.

[15] Jin S, et al. Seismic fragility analysis of nuclear containment structure using Bayesian logistic regression model. Soil Dynam Earthq Eng Mar. 2024;178:108435.

[16] Porter K, Kennedy R, Bachman R. Creating fragility functions for performance-based earthquake engineering. Earthq Spectra 2007;23(2):471–89.

[17] Baker JW. Efficient analytical fragility function fitting using dynamic structural analysis. Earthq Spectra Feb. 2015;31(1):579–99. https://doi.org/10.1193/021113EQS025M.

[18] Jin C, Chi S. Seismic fragility analysis of high earth-rockfill dams considering the number of ground motion records. Math Probl Eng 2019;2019(1):6958643.

[19] Rapti I, Lopez-Caballero F, Modaressi-Farahmand-Razavi A, Foucault A, Voldoire F. Liquefaction analysis and damage evaluation of embankment-type structures. Acta Geotech Oct. 2018;13(5):1041–59. https://doi.org/10.1007/s11440-018-0631-z.

[20] Khalil C, Lopez-caballero F. Effect of synthetic ground motions on the liquefaction induced settlements. 2019. South Korea.

[21] Lopez-Caballero F, Khalil C. Vulnerability assessment for earthquake liquefaction–induced settlements of an embankment using Gaussian processes. ASCE-ASME J Risk Uncertain Eng Syst Part Civ Eng Jun. 2018;4(2):04018010.

[22] Khalil C, Lopez-Caballero F. Lifetime response of a liquefiable soil foundation-embankment system subjected to sequences of mainshocks and aftershocks. Soil Dynam Earthq Eng Oct. 2023;173:108107. https://doi.org/10.1016/j.soildyn.2023.108107.

[23] Jiang S-H, Wang L, Ouyang S, Huang J, Liu Y. A comparative study of Bayesian inverse analyses of spatially varying soil parameters for slope reliability updating. Georisk Assess Manag Risk Eng Syst Geohazards Oct. 2022;16(4):746–65.

[24] Ma Y, Li J, Wang D, Mi J, Dai K. Probabilistic prediction of hysteretic curves of corroded reinforced concrete columns based on Bayesian theory. Soil Dynam Earthq Eng Jun. 2025;193:109308. https://doi.org/10.1016/j.soildyn.2025.109308.

[25] Rong M, Zhang Y, Li X, Ni P, Wang J. Bayesian inversion method for soil layer velocity structures based on the earthquake horizontal-to-vertical spectral ratio and its applications. Soil Dynam Earthq Eng Apr. 2026;203:110034. https://doi.org/10.1016/j.soildyn.2025.110034.

[26] Yang H, Xue X. Bayesian framework for evaluating spatial distribution of soil liquefaction based on CPT data. Soil Dynam Earthq Eng Dec. 2025;199:109657.

[27] Kruschke J. Doing bayesian data analysis: a tutorial with R, JAGS, and Stan. Academic Press; 2014.

[28] Gelman A, Carlin JB, Stern HS, Dunson DB, Vehtari A, Rubin DB. Bayesian data analysis. third ed. New York: Chapman and Hall/CRC; 2013. https://doi.org/10.1201/b16018.
[29] Huang X, Liu W, Guo Q, Tan J. Prediction method for the dynamic response of expressway lateritic soil subgrades on the basis of Bayesian optimization CatBoost. Soil Dynam Earthq Eng Nov. 2024;186:108943. https://doi.org/10.1016/j.soildyn.2024.108943.
[30] Sadeghzadeh S, Sberna AP, Di Trapani F, Demartino C. Enhancing seismic site response analyses: tuning soil properties via genetic algorithms and Bayesian model updating from downhole array data. Soil Dynam Earthq Eng Jan. 2026;200:109773.
[31] Taheri S, Mohammadi RK. Probabilistic prediction of engineering demand parameters using Bayesian inference approach. Soil Dynam Earthq Eng Oct. 2022;161:107320.
[32] Du-bo W, Han-long LIU, Tao YU, Gui Y. Seismic fragility analysis for earth-rockfill dams based on deformation. Chin J Geotech Eng May 2013;35(5):814–9.
[33] Cockburn G, Tesfamariam S. Earthquake disaster risk index for Canadian cities using Bayesian belief networks. Georisk Assess Manag Risk Eng Syst Geohazards Jun. 2012;6(2):128–40. https://doi.org/10.1080/17499518.2011.650147.
[34] van der Zon J, Flessati L, Mavritsakis A, Habets C, Schweckendiek T, Roubos A. Identifying unaccounted capacity of ground anchors through Bayesian updating: a case study. Georisk Assess Manag Risk Eng Syst Geohazards Jul. 2025;19(3):682–97.
[35] He J, Rathje E. Database for the development of capacity relationships for Earth dam. DesignSafe-CI; May 24, 2023. https://doi.org/10.17603/ds2-pwtv-p173.
[36] Tekeste GG, Correia AA, Costa AG. Bayesian updating of seismic fragility curves through experimental tests. Bull Earthq Eng Mar. 2023;21(4):1943–76.
[37] Jiang H, Peng C. Bayesian update of fragility curves for equipment failure probability in seismic probabilistic safety assessment in nuclear power plant. Ann Nucl Energy Jun. 2024;201:110436. https://doi.org/10.1016/j.anucene.2024.110436.
[38] Chen X, Zhu H, Li X, Lin X, Wang X. Probabilistic performance prediction of shield tunnels in operation through data mining. Sustain Cities Soc Jan. 2019;44:819–29.
[39] Xie Y, Zhang Y, Liang F. Crash injury severity analysis using bayesian ordered probit models. J Transport Eng Jan. 2009;135(1):18–25.
[40] Van Biesbroeck A, Gauchy C, Feau C, Garnier J. Reference prior for Bayesian estimation of seismic fragility curves. Probab Eng Mech Apr. 2024;76:103622.
[41] Straub D, Papaioannou I. Bayesian updating with structural reliability methods. J Eng Mech Mar. 2015;141(3):04014134. https://doi.org/10.1061/(ASCE)EM.1943-7889.0000839.
[42] Cornell CA, Jalayer F, Hamburger RO, Foutch DA. Probabilistic basis for 2000 SAC federal emergency management agency steel moment frame guidelines. J Struct Eng Apr. 2002;128(4):526–33. https://doi.org/10.1061/(ASCE)0733-9445(2002)128:4(526).
[43] Röver C, et al. On weakly informative prior distributions for the heterogeneity parameter in Bayesian random-effects meta-analysis. Res Synth Methods 2021;12(4):448–74.
[44] Hastings WK. Monte Carlo sampling methods using Markov chains and their applications. Biometrika Apr. 1970;57(1):97–109. https://doi.org/10.1093/biomet/57.1.97.
[45] Metropolis N, Rosenbluth AW, Rosenbluth MN, Teller AH, Teller E. Equation of state calculations by fast computing machines. J Chem Phys Jun. 1953;21(6):1087–92. https://doi.org/10.1063/1.1699114.
[46] Robert C, Casella G. Monte Carlo statistical methods. New York: Springer; 2005.
[47] Vehtari A, Gelman A, Gabry J. Practical Bayesian model evaluation using leave-one-out cross-validation and WAIC. Stat Comput Sep. 2017;27(5):1413–32.
[48] Sriwastava A, Reichert P. Sensitivity analysis of Bayesian estimates of value function parameters to priors using imprecise probabilities. J Choice Model Dec. 2025;57:100581. https://doi.org/10.1016/j.jocm.2025.100581.
[49] Canavos GC, Smith CH. Sensitivity of a bayesian inference to prior assumptions. J Stat Comput Simulat Aug. 1986;25(1–2):25–36. https://doi.org/10.1080/00949658608810922.
[50] Riabiz M, et al. Optimal thinning of MCMC output. J R Stat Soc, Ser B Stat Methodol Sep. 2022;84(4):1059–81. https://doi.org/10.1111/rssb.12503.
[51] Owen AB. Statistically efficient thinning of a markov chain sampler. J Comput Graph Stat Jul. 2017;26(3):738–44. https://doi.org/10.1080/10618600.2017.1336446.
[52] Bommer JJ, Acevedo AB. The use of real earthquake accelerograms as input to dynamic analysis. J Earthq Eng Jan. 2004;8(sup001):43–91.
[53] Giovinazzi S, Lagomarsino S. A macroseismic method for the vulnerability assessment of buildings. Presented at the 13th world conference on earthquake engineering. B.C., Canada: Vancouver; 2004.
[54] FEMA, Fema F. HAZUS-MH-MR1, multi-hazard loss estimation methodology. 2003. 2003.
[55] Guo X, Dias D, Pan Q. Probabilistic stability analysis of an embankment dam considering soil spatial variability. Comput Geotech Sep. 2019;113:103093.
[56] GEO-SLOPE International Ltd. GeoStudio 2024 [Computer software]. Seequent; 2024.
[57] Mouyeaux A, Carvajal C, Bressolette P, Peyras L, Breul P, Bacconnet C. Probabilistic stability analysis of an earth dam by Stochastic finite element method based on field data. Comput Geotech Sep. 2018;101:34–47. https://doi.org/10.1016/j.compgeo.2018.04.017.
[58] Lysmer J, Kuhlemeyer RL. Finite dynamic model for infinite media. J Eng Mech Div Aug. 1969;95(4):859–77. https://doi.org/10.1061/JMCEA3.0001144.
[59] Burman A, Nayak Parsuram, Agrawal P, Maity Damodar. Coupled gravity dam–foundation analysis using a simplified direct method of soil–structure interaction. Soil Dynam Earthq Eng 2011;34(1):62–8.
[60] Chakraborty R, Dey A. Probabilistic assessment of seismic response of toe-excavated partially saturated hillslopes. Indian Geotech J Feb. 2024;54(1):196–209.
[61] Ahmad M, Ray R. The dynamic properties of sand under torsion: a literature review. Geotechnics 2023;3(2):480–514.
[62] Vucetic M, Dobry R. Effect of soil plasticity on cyclic response. J Geotechnical Eng 1991;117(1):89–107.
[63] Hu H, Gan G, Cui L, Xia T, Wang L, Han X. Nonparametric representation for seismic fragility assessment of Earth dams with spatially variable soil properties. Int J GeoMech Aug. 2023;23(8):04023108. https://doi.org/10.1061/IJGNAI.GMENG-7266.
[64] Hardin BO, Black WL. Vibration modulus of normally consolidated clay. J Soil Mech Found Div 1968;94(2):353–69.
[65] Hardin BO, Drnevich VP. Shear modulus and damping in soils: measurement and parameter effects (terzaghi lecture). J Soil Mech Found Div 1972;98(6):603–24.
[66] Hardin BO. The nature of stress-strain behavior for soils. In: From volume I of earthquake engineering and soil Dynamics–Proceedings of the ASCE geotechnical engineering division specialty conference, June 19-21, 1978; 1978, June. Pasadena, California. Sponsored by Geotechnical Engineering Division of ASCE in cooperation with: (No. Proceeding).
[67] Mayne PW, Rix GJ. G max-qc relationships for clays. Geotech Test J 1993;16(1):54–60.
[68] Seed HB. Soil moduli and damping factors for dynamic response analyses, EERC-70. Report; 1970.
[69] Phillips C, Hashash YMA. Damping formulation for nonlinear 1D site response analyses. Soil Dynam Earthq Eng Jul. 2009;29(7):1143–58.
[70] Hu H, Fu C, Bao Y, et al. Seismic fragility assessment of slopes with scalar-valued and vector-valued earthquake intensity measures. Acta Geotech 2025;20:3871–86.
[71] Ahmed T, Alel MNA, Ab Kadir MA, Rahim A, Shahrin MI. Seismic fragility assessment of embankment: a displacement-based approach using dynamic finite element model analysis. In: IOP conference series: earth and environmental science, 1369. IOP Publishing; 2024, June, 012009. No. 1.
[72] Kouroussis G, Verlinden O, Conti C. Finite-dynamic model for infinite media: corrected solution of viscous boundary efficiency. J Eng Mech Jul. 2011;137(7):509–11.
[73] Chiaradonna A. Defining the boundary conditions for seismic response analysis—A practical review of some widely-used codes. Geosciences Feb. 2022;12(2):83.
[74] Seed HB, Lee KL, Idriss IM, Makdisi FI. The slides in the San Fernando Dams during the earthquake of February 9, 1971. J Geotech Eng Div Jul. 1975;101(7):651–88. https://doi.org/10.1061/AJGEB6.0000178.
[75] Lee KZZ, Jensen N, Gillette DR, Wittwer DT. Seismic deformation analysis of embankment dams using simplified total-stress approach. J Geotech Geoenviron Eng 2019;145(10):04019076.
[76] Beaty MH, Byrne PM. Liquefaction and deformation analyses using a total stress approach. J Geotech Geoenviron Eng 2008;134(8):1059–72.
[77] Boulanger RW, Montgomery J. Nonlinear deformation analyses of an embankment dam on a spatially variable liquefiable deposit. Soil Dynam Earthq Eng 2016;91:222–33.
[78] Seed HB. Ground motions and soil liquefaction during earthquakes. Earthquake engineering research institute; 1982.
[79] Jana K, Sarkar R, Bhattacharya S. Effects of liquefaction on seismic fragility of monopile-supported multi-megawatt offshore wind turbines for Indian coastal regions. Structures, 80. Elsevier; 2025, October, 109694.
[80] Chakraborty A, Sawant VA. Fragility assessment of highway embankment resting on liquefaction-susceptible soil. Comput Geotech Sep. 2023;161:105568.
[81] Amorosi A, Boldini D, Elia G. Parametric study on seismic ground response by finite element modelling. Comput Geotech Jun. 2010;37(4):515–28.
[82] Park K-C, Nguyen V-Q, Kim J-H, Park D, Choi B-H. Estimation of seismically-induced crest settlement of Earth core rockfill dams. Appl Sci Jan. 2019;9(20):4343. https://doi.org/10.3390/app9204343.
[83] Harder Jr LF, Bray JD, Volpe RL, Rodda KV. Performance of earth dams during the Loma Prieta earthquake. US Geological Survey professional paper; 1998. p. 3–26.
[84] Dakoulas P, Gazetas G. A class of inhomogeneous shear models for seismic response of dams and embankments. Int J Soil Dynam Earthq Eng 1985;4(4):166–82.
[85] Ren H, Wu Y, Li W, Cai X. Seismic damage assessment using frequency characteristics of acceleration records in centrifugal vibration table tests for CSG dam. Soil Dynam Earthq Eng 2026;203:110000.
[86] Newmark NM. Effects of earthquakes on dams and embankments. Geotechnique Jun. 1965;15(2):139–60. https://doi.org/10.1680/geot.1965.15.2.139.
[87] Gazetas G. Seismic response of earth dams: some recent developments. Soil Dynam Earthq Eng Jan. 1987;6(1):2–47. https://doi.org/10.1016/0267-7261(87)90008-X.
[88] Seismosoft. SeismoSignal (Version 2024) [Computer software] Seismosoft 2024.